This is to certify that the
thesis entitled

DEFECT PROFILING IN STEAM GENERATOR TUBES USING MULTI-FREQUENCY EDDY CURRENT INSPECTION

presented by

Uduebho Oseghale Olumese

has been accepted towards fulfillment
of the requirements for the

Master of Science	degree in	Electrical Engineering and Computer Engineering

Lalita Udpa
Major Professor's Signature

July 28, 2007
Date

DEFECT PROFILING IN STEAM GENERATOR TUBES USING MULTI-FREQUENCY EDDY CURRENT INSPECTION

By

Uduebho Oseghale Olumese

A THESIS

Submitted to
Michigan State University
in partial fulfillment of the requirements
for the degree of

MASTER OF SCIENCE

Department of Electrical & Computer Engineering
2007

ABSTRACT

DEFECT PROFILING IN STEAM GENERATOR TUBES USING MULTI-FREQUENCY EDDY CURRENT INSPECTION

By

Uduebho Oseghale Olumese

Multi-frequency eddy current technique is one of the widely used Non-destructive evaluation techniques for steam generator tube inspection in nuclear power industry. The multi-frequency technique for depth profiling is essentially a multi-dimensional data fusion scheme which tends to mitigate the effect of error-prone single-dimension eddy current features due to noise and improves defect identification, classification and characterization of the eddy current data. In this research, the performance of traditional defect characterization algorithms are investigated alongside a novel defect depth profiling procedure using a radial basis function neural network by employing the following two step approach

- The length of the defect is estimated by setting an adaptive threshold on the magnitude distribution in the region of interest engulfing potential defects.
- The inversion of the signal features in the defect region to predict a depth profile. The vehicle for this inversion is the radial basis function neural network.

The thesis also discusses noise removal in eddy current data and their limitations when deployed for depth profiling purposes.

DEDICATION

This thesis is dedicated to God Almighty through Whom all things are possible.

ACKNOWLEDGEMENTS

I would like to gratefully acknowledge the enthusiastic supervision and academic mentoring of Dr. Lalita Udpa during this work. You gave wings to my dreams. I also thank Dr. Ramuhalli Pradeep for the technical discussions he provided and Ameet Joshi who contributed to the development of the algorithms in this research work. I also wish to express my gratitude to Mr James Benson at the Electric Power Research Institute for his support. The testing and validation of the algorithms was performed by Steve Brown to whom I am grateful.

Finally, I am forever indebted to my parents and Onome Ewere, my fiancée, for their understanding, endless patience and encouragement when it was most required. I am also grateful to Napoleon Ifie and my siblings for their support.

STATEMENT OF AUTHENTICATION

The work presented in this thesis is, to the best of my knowledge and belief, original, except as acknowledged in the text. I hereby declare that I have not submitted this material, either in whole or in part, for a degree at this or any other institution.

……………………………………………..
(Signature)

TABLE OF CONTENTS

CHAPTER 1: INTRODUCTION TO NONDESTRUCTIVE EVALUATION

CHAPTER 2

CHAPTER 3: EDDY CURRENT PROBE DATA ANALYSIS

CHAPTER 4: ARTIFICIAL NEURAL NETWORKS

CHAPTER 5: EXPERIMENTAL ANALYSIS AND RESULTS

LIST OF TABLES

LIST OF FIGURES

** Some images in this thesis are presented in color

KEY TO ABBREVIATIONS AND SYMBOLS

ROI – Region of interest
MET – Metallographic Depth Profile
NDE – Non-Destructive Evaluation
ETSS – Examination Technique Specification Sheet
Δ - Difference operator

CHAPTER 1 Introduction to Nondestructive Evaluation

1.1 INTRODUCTION

Non-Destructive Testing (NDT) is defined as the structural assessment of an object, material or system without damaging its future utility. In other words, NDT is carried out in such a way as to preserve the specimen's structural integrity. In a general NDT system, an energy source is used to probe the test object with an aim to measure the interaction of the energy with the test object using a receiving transducer [3]. The measured signal contains information about structural flaws in the object. The signal thus collected undergoes a series of signal processing stages that boost the signal to noise ratio for accurate flaw detection while minimizing false alarm. Subsequently, classification algorithms are employed for flaw characterization purposes.

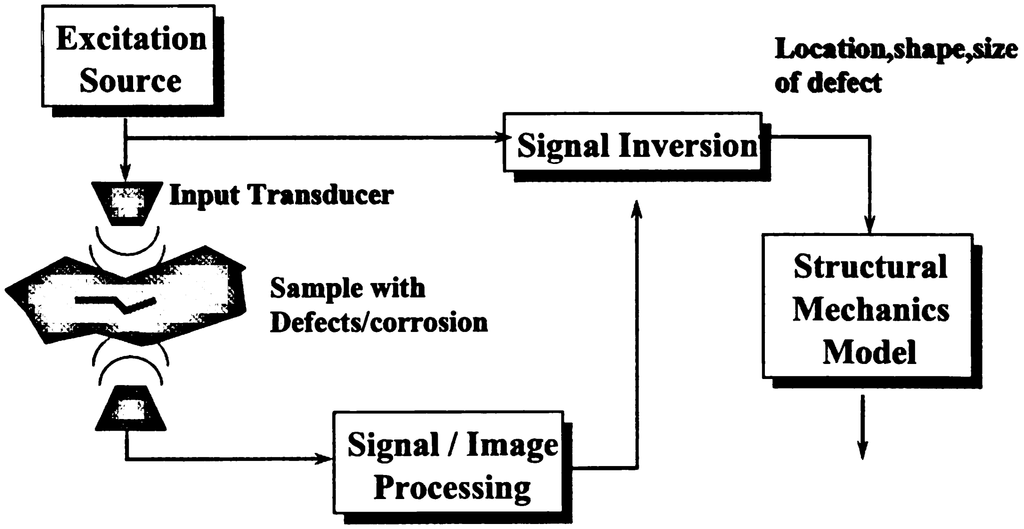

Figure 1.1 Non-Destructive Evaluation System

1.2 Typical Methods for Nondestructive Testing

The National Materials Advisory Board (NMAB) Ad Hoc Committee on Nondestructive Evaluation adopted a system [1, 2] that classifies nondestructive methods into six major categories: visual, penetrating radiation, magnetic-electrical, mechanical vibration, thermal and chemical-electrochemical. A version of the taxonomy of inspection methods is presented in Table 1.1, with additional categories included to cover new methods [13].

Table 1.1 NDE Classification System

Basic Categories	**Objectives**
Mechanical and optical	color, cracks, dimensions, film thickness, reflectivity, strain distribution and magnitude, surface finish, surface flaws, through-cracks
Penetrating radiation	cracks, density and chemistry variations, elemental distribution, foreign objects, inclusions, micro-porosity, misalignment, missing parts, segregation, service degradation, shrinkage, thickness, voids
Electromagnetic and electronic	alloy content, anisotropy, cavities, cold work, local strain, hardness, composition, contamination, corrosion, cracks, crack depth, crystal structure, electrical and thermal conductivities, flakes, heat treatment, hot tears, inclusions, ion concentrations, laps, lattice strain, layer thickness, moisture content, polarization, seams, segregation, shrinkage, state of cure, tensile strength, thickness, disbands
Sonic and ultrasonic	crack initiation and propagation, cracks, voids, damping factor, degree of cure, degree of impregnation, degree of sintering, delaminations, density, dimensions, elastic moduli, grain size, inclusions, mechanical degradation, misalignment, porosity, radiation degradation, structure of composites, surface stress, tensile, shear and compressive strength, disbonds, wear
Thermal and infrared	bonding, composition, emissivity, heat contours, plating thickness, porosity, reflectivity, stress, thermal conductivity, thickness, voids
Chemical and analytical	alloy identification, composition, cracks, elemental analysis and distribution, grain size, inclusions, macrostructure, porosity, segregation, surface anomalies

Table 1.1 continued

Auxiliary Categories	**Objectives**
Image generation	dimensional variations, dynamic performance, anomaly characterization and definition, anomaly distribution, anomaly propagation, magnetic field configurations
Signal image analysis	data selection, processing and display, anomaly mapping, correlation and identification, image enhancement, separation of multiple variables, signature analysis

The first six categories involve basic physical processes that require transfer of energy to the object being tested. The auxillary category includes processes that provide for transfer and accumulation of information, and evaluation of the raw signals and images common to nondestructive testing methods. Commonly used methods include ultrasonic, magnetic flux leakage, radiographic, penetrant and eddy current techniques. A brief introduction to some of these methods follows.

1.2.1 Ultrasonic NDT

Based on the principle that solid materials are good conductors of sound waves and that waves are reflected by interfaces or internal material dislocations, beams of high-frequency sound waves are introduced into the test object for detection of subsurface flaws in the material. The transducer used in ultrasonic NDE is usually a piezoelectric element excited by an extremely short electrical discharge, to generate an ultrasonic pulse. Conversely, an electrical signal is generated when it receives an ultrasonic signal. In general, the probe is coupled to the test material via air, gel or water to minimize signal attenuation and back scattering at the probe-material interface. As sound energy propagates through the material, a fraction of the energy is reflected back when discontinuities are encountered in the wave path. These reflected waves due to discontinuities in the object are used for detection of the flaw. The reflected beam is subsequently analyzed to define the presence and location of flaws or discontinuities.

The most commonly used ultrasonic testing technique is in the pulse-echo mode, wherein sound is introduced into a test object and reflections (echoes) are returned to a receiver from internal imperfections or from the part's geometrical surfaces.

The merits of ultrasonic inspection include sensitivity to both surface and subsurface discontinuities, superior depth of penetration when compared to other methods, higher accuracy in determining the position, size, and shape of defect and minimal test object preparation. However, ultrasonic inspection also has its drawbacks. Defects oriented parallel to the sound beam may be undetected. Accessibility of the surface for inspection is also an issue. Finally, the skills and training required for ultrasonic inspection is more extensive compared to other methods. Applications include inspections for voids, cracks, and laminations, inspections of welds and thickness measurements [3].

1.2.2 Radiographic NDE

This technique involves the use of penetrating gamma or X-radiation to examine parts and products for imperfections. An X-ray machine or radioactive isotope is used as a source of radiation. Energy from the source propagates through a test specimen and the radiation is directed through a part and onto film in order to project an image on the receiver (X-ray film) or recording plane on the opposite side. Significant differences in the received signal intensity can be interpreted in terms of defects and anomalies in the test object. Any imperfection in the test object is indicated as density changes in the film in the same manner as how medical X-ray shows fractured bones [3]. All abnormalities in the test object are viewed on the recording plane as light or dark spots compared to the rest of the material depending on the properties of the material and anomaly.

Radiographic applications fall into two distinct categories, namely, evaluation of material properties and evaluation of manufacturing and assembly properties. Material property evaluation includes the determination of composition, density, uniformity, and cell or particle size. Manufacturing and assembly property evaluation is normally concerned with dimensions, flaws (voids, inclusions, and cracks), bond integrity (welds, brazes, etc.), and verification of proper assembly of component pieces.

1.2.3 Electromagnetic NDT

In electromagnetic NDT methods, the energy source is electric and magnetic fields. Some of the popular electromagnetic methods are potential drop, magneto-static leakage field, and eddy current methods. The magnetic leakage field technique uses direct current as the excitation source, while the eddy current method uses an alternating current. In this thesis work, the particular area of interest in electromagnetic NDT techniques is the eddy current testing method. The eddy current induced in the test specimen are affected by the variation of one or more properties such as magnetic permeability, electric permittivity or electric conductivity of the test specimen.

Consequently the measured signal carries information about the shape, size and location of defects in conducting materials.

1.3 Eddy Current Inspections of Heat Exchange Tubes in Nuclear Power Plants

Eddy current testing methods are widely used for inspecting heat – exchange tubes in steam generators in nuclear power plants. Figure 1.1 shows the typical layout of the heat transfer system in nuclear power plants. Nuclear fission in the reactor generates heat energy which is conveyed via the primary coolant circulating within the nuclear vessel. The primary coolant dissipates the heat energy into a water-steam mixture as it is circulated through a set of tubes in the steam generator. The high-pressure vapor is forced through the secondary loop and is used to drive the steam turbines. While in primary loop, the coolant is radioactive, the coolant in the secondary loop is not radioactive. It is critical to keep the radioactive coolant from contaminating the non-radioactive coolant water [5]. Frequent inspection of the steam generator tubes is therefore mandatory in order to keep the whole system free from radioactive leakage.

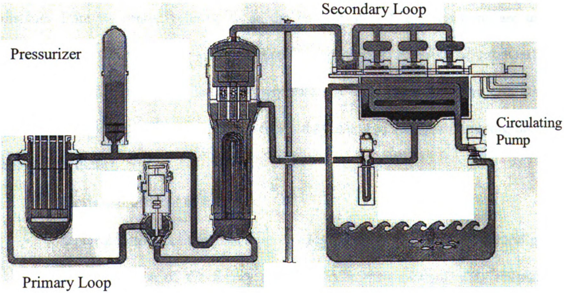

Figure 1.2 Heat transfer system in nuclear power plants [5]

During the tube inspection, an eddy current probe is inserted at one end of the heat exchange tube after which it translates at constant velocity towards the other tube end. As the eddy current probe describes a raster scan within the tube, its impedance is measured as a function of time (or location in the tube). The data obtained in the inspection process must be calibrated and compensated for the variation in probe characteristics and instrument configuration settings. The signal is then analyzed and interpreted in terms of location, shape and size of defect in tube wall. This thesis describes the development and evaluation of procedures for profiling defects in the steam generator tube wall.

1.2 Scope of Thesis

This thesis addresses the problem of defect characterization using neural network interpolation techniques. The radial basis function neural network is the framework in which features from eddy current data are analyzed for defect characterization purposes. A radial basis function (RBF) is a real-valued function whose value depends only on the distance from its center, referred to as the basis center. These functions are used in function approximation, time series prediction, and control. A weighted combination of radial basis functions can be used to interpolate any continuous function with arbitrary accuracy on a compact interval. In this thesis they are used for approximating the depth profile of a defect.

This thesis is organized as follows:

- Chapter 2 introduces the principles of eddy current testing techniques and gives a brief description of the theory of the eddy current method. This chapter also includes the description of the measurement system used to inspect the steam generator tubes in nuclear power plants. In addition, a description of data analysis system including data preprocessing and signal enhancement is included.

- Chapter 3 gives an overview of conventional defect profiling methods. The merits and demerits of these techniques are discussed in this chapter. The radial basis function theory is described alongside the implementation of the concept for the purpose of defect profiling.
- Chapter 4 describes the neural network and the radial basis function neural network in particular. The method of implementation of the radial basis function neural network for steam generator tube depth profiling is explained.
- Chapter 5 first provides a description, comparison and conclusion of the experimental results obtained using conventional defect profiling methods and the radial basis function interpolation approach. The effect of noise and eddy current data filtering on the defect profiling method is also demonstrated.

CHAPTER 2

2.1 **Principles of Eddy Current Testing and Its Application in Steam Generator Tube Inspection [14]**

The basic principle underlying eddy current inspection methods can be illustrated with a simple arrangement shown in Figure 2.1. When a coil carrying an alternating current is brought in close proximity to an electrically conducting, non-ferromagnetic test specimen, an alternating magnetic field is established. This field causes currents to be induced in the conducting test specimen in accordance with Faraday's law of electromagnetic induction. The induced currents are called eddy currents since they follow closed circulatory patterns that are similar to eddies found in water bodies. The alternating eddy current, in turn, establishes a field whose direction is opposite to that of the original or primary field. Consequently, the net flux linkages associated with the coil decreases. Since the inductance of a coil is defined as the number of flux linkages per ampere, the effective inductance of the coil decreases relative to its value if it were to be suspended in air. The presence of eddy currents in the test specimen also results in a resistive power loss. The effect of this power loss manifests itself as a small increase in the effective resistance of the coil. An exaggerated view of the changes in the terminal characteristics of the coil is shown in Figure 2.2 where the variation in resistance and inductance is plotted in the impedance plane. When a flaw whose conductivity differs from that of the host specimen is present, the current distribution is altered. Consequently, the impedance of the coil changes relative to its value obtained with an unflawed specimen, as shown in Figure 2.2. Systems that are capable of monitoring the changes in impedance can, therefore, be used to detect flaws in a specimen that is scanned by a coil.

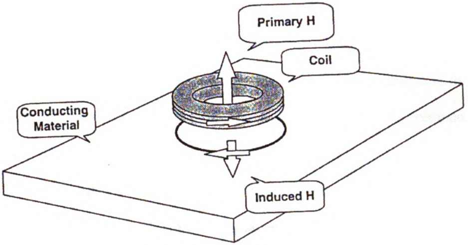

Figure 2.1 Principles of Eddy Current Testing [3]

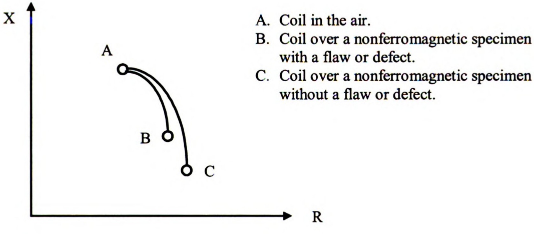

Figure 2.2 Impedance plane trajectory of a coil over a non-ferromagnetic specimen [3]

2.2 Eddy Current Transducers

Eddy current transducers may be categorized according to coil configuration into absolute and differential eddy current transducers [5]. Absolute eddy current transducers, usually consisting of a single coil, directly measures the absolute coil impedance rather than its differential value and can detect both gradual and sharp changes. However a disadvantage in using absolute transducers is that small changes of the impedance due to a flaw are often superimposed on the large value [5]. The obvious limitation of this form of inspection is that no difference in cross-section occurs if a defect is continuous for the whole length of the material [7].

Furthermore, lift – off and probe wobble can mask the small changes of coil impedance due to defects thereby making signal analysis difficult.

In contrast, differential eddy current transducers consist of a pair of coils with a configuration such that the net value of the impedance is the vector difference of the individual coil impedances. Undesirable effects due to lift – off and probe wobble is eliminated because they generally have the same impact on both coils [5]. In general, differential eddy current transducers more sensitive to impedance change than absolute eddy current transducers.

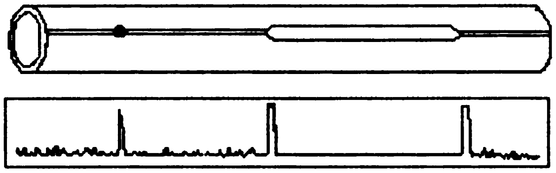

Differential output

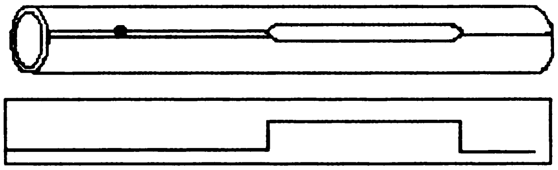

Absolute output

Figure 2.3 Differential and absolute outputs [7]

2.3 Multi-frequency Eddy Current Signals

2.3.1 Skin Effect

The skin effect is the tendency of an alternating electric current (AC) to distribute itself within a conductor so that the current density near the surface of the conductor is greater than that at its core. That is, the electric current tends to flow at the "skin" of the conductor. The skin effect causes the effective resistance of the conductor to increase with the frequency of the current [14].

Mathematically, the current density J in an *infinitely thick* plane conductor decreases exponentially with depth δ from the surface, as follows:

$$J = J_S \, e^{-\delta/d} \quad \ldots\ldots\ldots\ldots\ldots\ldots (2)$$

where d is a constant called the *skin depth*. This is defined as the depth below the surface of the conductor at which the current density decays to 1/e (about 0.37) of the current density at the surface (J_S). It can be calculated as follows:

$$d = \sqrt{\frac{2\rho}{\omega\mu}} \qquad \text{..................(3)}$$

where

ρ = resistivity of conductor

ω = angular frequency of current = $2\pi \times$ frequency

μ = absolute magnetic permeability of conductor and is equivalent to the product of μ_0 and μ_r, where μ_0 is the permeability of free space and μ_r is the relative permeabilty of the conductor.

Due to skin effect in test specimen, single frequency eddy current testing does not provide an exhaustive evaluation of steam generator tubes at all tube depths. However, multi-frequency eddy current testing circumvents this limitation by providing extra characteristic information at various portions of the tube depth. This is because lower frequencies have larger skin depths and hence detect strong indications of support structures that are located outside of the tube such as support plates. On the other hand, higher frequencies have shallower skin depths and detect strong indications of flaws located closer to the surface. Multi-frequency eddy current testing involves measuring coil impedance simultaneously using several excitation frequencies in one probe pull [6]. The availability of multi-frequency data also allows for the suppression of undesired discontinuities and enhances flaw classification and characterization results.

2.3.2 Eddy Current Testing Probes

Three types of multi-frequency probes are used in practice namely the bobbin coil probe, rotating probe coil and array probe. The bobbin coil probe consists of two nominally identical coils connected in a differential mode and excited at multiple frequencies. Due to the relatively low resolution in raster scan, the bobbin coil probe is mainly used for the initial detection of possible degradation to quickly determine those areas of the tube requiring additional inspection with other types of probe that have improved ability to size and characterize degradation, such as rotating probes [6].

The array probe is a relatively newer probe type and is designed to provide higher resolution coverage of the tube with inspection speeds approaching that of bobbin coil inspection. However, the resolution of the probe, especially along the circumferential direction, is poor [6].

From a resolution measurement perspective, the rotating probe coil (RPC) is the most superior eddy current probe. The eddy current data used for the implementation of the depth profiling methods described in subsequent chapters were obtained using the rotating probe coil. This is large due to the relatively high resolution offered by the system. Figure 2.5 shows a probe consisting of a low frequency pancake coil, plus-point coil and high-frequency pancake coil rotating and translating inside a tube. Typical signals generated by a multi-frequency-rotating probe testing system are shown in Figure 2.6 where the trigger signal marks the probe circumferential position and is used to transform the one-dimensional signal to form a two-dimensional image. The low frequency channel is usually designed to locate external structures such as tube support plates (TSP) and tube sheets (TS).

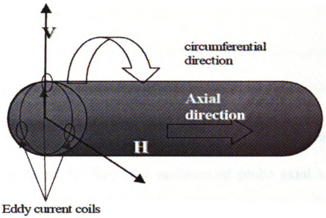

Figure 2.4 Tube inspection using the rotating probe coil

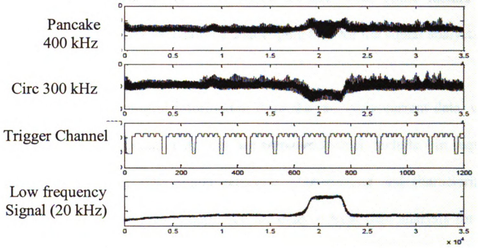

Figure 2.5 Typical trigger channel signal alongside signals from pancake and plus point coils. [6]

The next chapter introduces the eddy current signal pre-preprocessing stage and the sequence of step taken to identify regions of interest. Conventional depth profiling methods is also explained.

CHAPTER 3 Eddy Current Probe Data Analysis

3.1 Introduction

Several issues in the eddy current inspection system pose difficulty in the characterization of flaws. These include poor resolution of the probe raster scan relative to the physical dimensions of the flaw, the variation of probe axial velocity about the nominal value and the quantization errors introduced when the analog eddy current signal is sampled and digitized. Furthermore, additive noise generated due to corrosion deposits, shot and thermal noise introduce errors in signal measurement. These factors act in combination to make flaw characterization a challenging task for the signal analyst.

In order to extract meaningful information from the raw eddy current data, various techniques and data manipulating operations are employed which include - in sequential order - signal preprocessing, flaw signal detection, classification and characterization. Figure 3.1 shows a schematic of the approach for eddy current data analysis for steam generator tube evaluation

. 3.1. 1 Signal Preprocessing

This stage of the data analysis includes signal processing algorithms that perform signal synchronization and calibration. The rotating probe coil system comprises three different probe types, namely pancake, axial and circumferential plus point coil probes. Signals from each of these coils can be resolved into a vertical and horizontal channel. The axial and circumferential plus point coils are sensitive to axial and circumferential flaws, respectively, whereas pancake coils are sensitive to both types of flaws. Each of these coils is excited at multiple frequencies (typically 300 kHz, 200 kHz and 100 kHz) giving rise to about 28 – 32 channels altogether in the rotating probe coil system although some channels are redundant during the data acquisition process. The responses due to changes in coil impedance are sampled and saved in digital format for subsequent analysis.

An alternative configuration for the rotating probe uses two pancake and one plus-point coil probes. The plus point coil consists of two coils that are oriented orthogonal to each other [6]. The probe configurations, along with the excitation frequencies, are given in Table 3.1. Type A and B also possess axial encoder and trigger channels. Since each frequency component can be resolved into horizontal and vertical channels, there are 10 x 2 = 20 channels and 9 x 2 = 18 channels for type A and B respectively. In addition, two axial encoder channels and two trigger channels bring the effective number of active channels for type A and B to 24 and 22 channels respectively.

Table 3.1 Rotating probe configurations and inspection frequencies [6]

Probe types		Axial (kHz)	Circumferential	Pancake (0.115” diameter)	HF Pancake(0.080” diameter)	Plus Point
Type A	Excitation Frequencies (kHz)	400,300,200	400,300,200	400, 300, 200, 20		
Type B				300, 200, 100, 10	600, 300	300, 200, 100

** Type A and B possess trigger and axial encoder channels which are not included in table.

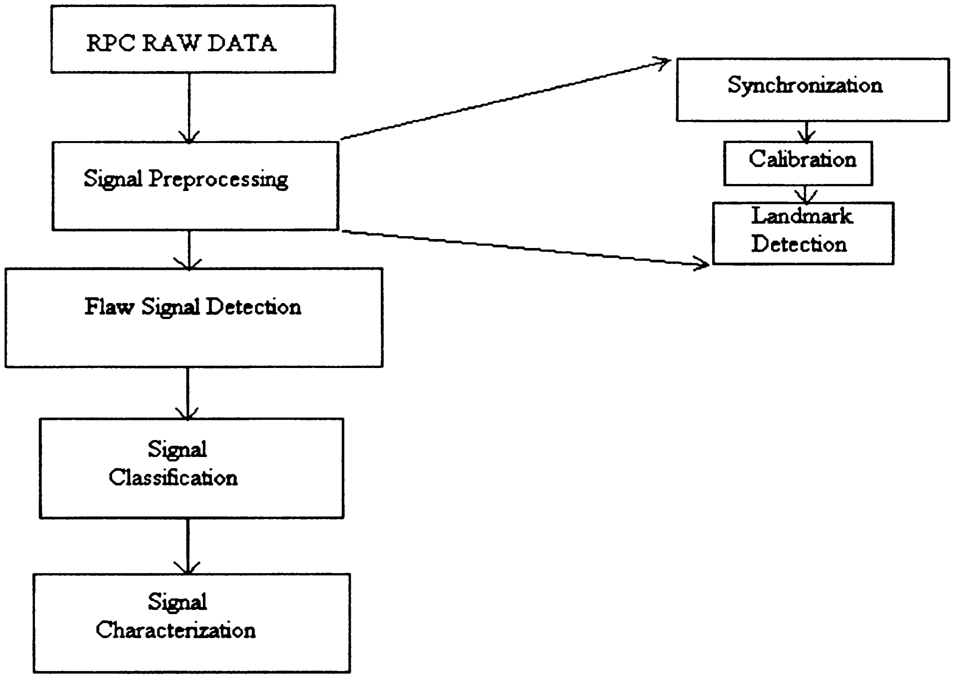

Figure 3.1 Schematic of Eddy Current Data Analysis

3.1.1.1 Synchronization

During tube inspection, the angular velocity of the RPC deviates minimally from its nominal value which, in turn, varies the number of samples per pitch as the probe translates along the length of the tube along a spiral path. In order to provide accurate synchronization points for each probe rotation, a trigger signal is generated simultaneously during probe operation. The trigger signal consists of four local synchronization pulses generated at 72°, 144°, 216° and 288° and a main synchronization pulse which occurs at 360° as shown in Figure 3.2. Figure 3.3 shows the wrapping of a one-dimensional eddy current signal into a two-dimensional representation.

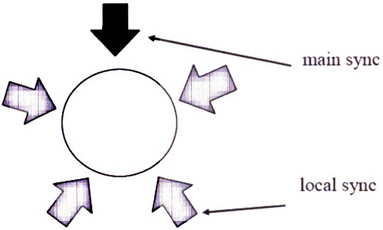

Figure 3.2 Coil configurations for trigger signal acquisition [6]

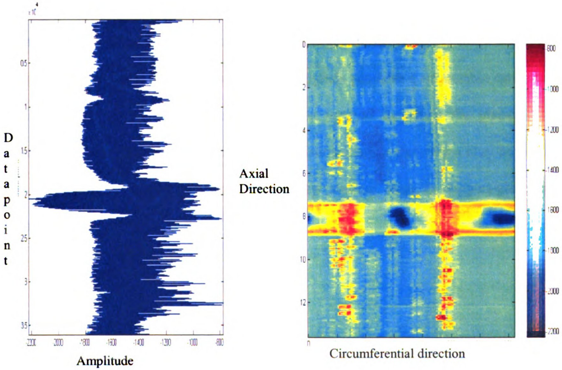

Figure 3.3 (Left) One-dimensional eddy current signal. (Right) Eddy current data representation in two-dimension after synchronization [6]

3.1.1.2 Calibration

For proper signal classification, it is imperative to determine properties such as voltage or phase of the test specimen signal, by measurement or comparison with signals from standard or reference specimen for which such signal properties are known. The reference specimen must possess similar metallurgical properties and physical dimensions as the material being inspected. Notches of known depths are introduced into the reference specimen in order to set a standard voltage and phase (by scaling and rotation respectively) for the reference notch signal, and in turn, the test specimen signal. This is essential in order that actual defects may be properly classified relative to the reference defects.

Proper classification and characterization of tube degradations is significantly dependent, among others, on signal phase. Phase lag of EC signals provides a reasonable estimate of the flaw depth and by setting a suitable phase interval in which the phase lag of characteristic flaw signals are contained, noise-discrimination algorithms may be used to reduce or eliminate false calls from pseudo-flaw sources such as support-plates and corrosive deposits.

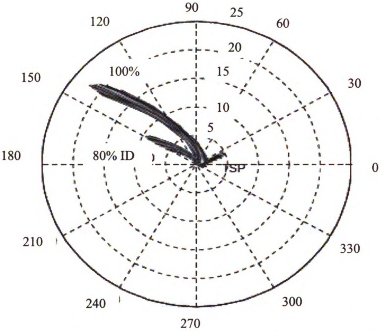

Figure 3.4 Impedance plane representation showing phase characteristics of 100% TW and 80% TW notch depth [6]

Figure 3.4 shows the impedance plane representation of a signal from a tube support plate, a 100% through wall (TW) flaw and an 80% inner diameter flaw [6]. The three signals have distinctive phase characteristics and this discriminating property can be used to determine the signal class and estimate depth of a flaw. In order to correct for possible phase offset due to differing probe responses and instrumentation setup, a phase calibration process is applied in industrial practice. As standard practice in industry, the phase corresponding to the 100% TW notch signal from the calibrating tube is rotated by a calibration phase factor *P* so that the resultant phase is 35° measured anti-clockwise from the negative x-axis. All test data from this calibration group undergoes the same extent of phase rotation given by *P*. This process is done independently for each frequency channel and coil type data.

In voltage scaling, the magnitude of the signal corresponding to a through-wall hole is first scaled to a fixed value giving a magnitude calibration factor *M*. The magnitude calibration factors, one for each frequency, are obtained by normalizing the maximum magnitude of the data from a 100% through-wall defect to a fixed value (usually 20 volts). The raw test data is then scaled by this same factor *M*, channel-by-channel. These magnitude scaling factors are computed for each coil at its primary frequency, typically the highest frequency (300 kHz) of coil excitation – and applied to the corresponding data in each channel [6]. In other words, the magnitude scaling factor obtained by calibrating the 300 kHz channel data (axial, circumferential and pancake) is applied to the 200 kHz and 100 kHz frequency channels.

3.1.1.3 Tube Support Segmentation

Since flaws are more likely to develop in the vicinity of support plates and other support structures, a low frequency measurement is first used to identify the location of such regions. Figure 3.5 shows a typical image obtained after segmentation. In practical eddy current testing, low frequency signals (usually at 10 kHz or 20 kHz) are used to locate external support structures such as tube support plates (TSP) or top of tube sheet signals (TTS). The data from the tube is then segmented into smaller regions around each support structure, which are analyzed separately with defect positions reported relative to these support structures.

As shown in Figure 3.5, an edge enhancement operation using a Sobel edge detector is employed to identify the edges of the TSP. The source image is represented by $f(x,y)$ where (x,y) denote the pixel locations of the image. The Sobel edge magnitude image

$|\nabla f(x,y)|$ is given by

$$\begin{aligned}|\nabla f(x,y)| &= \sqrt{\left(\frac{\partial f(x,y)}{\partial x}\right)^2 + \left(\frac{\partial f(x,y)}{\partial y}\right)^2} \\ &= \sqrt{(f \otimes s)^2 + (f \otimes t)^2}\end{aligned} \tag{3-1}$$

where s is the vertical edge detection filter, and t is a horizontal edge detection filter given below:

$$s = \begin{array}{|c|c|c|}\hline -1 & & 1 \\ \hline -2 & (x,y) & 2 \\ \hline -1 & & 1 \\ \hline \end{array} \qquad t = \begin{array}{|c|c|c|}\hline -1 & -2 & -1 \\ \hline & (x,y) & \\ \hline -1 & 2 & 1 \\ \hline \end{array} \tag{3-2}$$

The magnitude of $\nabla f(x,y)$ is then compared with a threshold T to determine candidate boundary points. Assuming x = 1,..., M and y = 1, ..., N; where M and N represent the number of columns and rows respectively in the two dimensional representation of the eddy current signal, then the threshold T is set at [23]

$$T = \sqrt{\beta\left(\mu^2 + \sigma^2\right)} \tag{3-3}$$

where β is a constant, μ is the mean, and σ is the variance of the image defined by

$$\mu = \frac{1}{MN}\sum_{x=1}^{M}\sum_{y=1}^{N} f(x,y), \quad \sigma = \frac{1}{MN}\sqrt{\sum_{x=1}^{M}\sum_{y=1}^{N}\left(f(x,y)-\mu\right)^2} \tag{3-4}$$

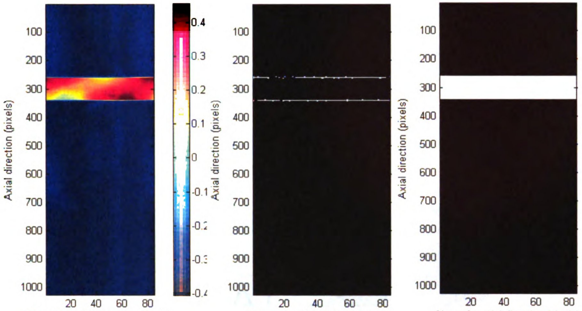

(a) (b) (c)

Figure 3.5 TSP Segmentation: (a) Low Frequency Signal, (b) Binary Image after Sobel edge detection, (c) Segmented Signal

The location of the TSP is then marked as the segment start point. Since the width of the TSP is fixed, it is also used as an axial scale standard to convert distance measures in image pixels to true distance (inches or millimeters).

3.1.1.4 Tube Support Suppression

Once support regions have been identified, signals from these structures need to be suppressed to enhance flaw signals (see figure 3.6). This suppression consists of two steps. The first step removes signals from structural discontinuities, such as tube support plates or tube sheets, by removing the median value in each circumferential revolution. Here, the median value is treated as the defect-free reference signal. The second step is to remove low frequency noise. The median value along the axial direction is subtracted to accomplish this objective. Let s_i be the signal from the i^{th} element along the column (circumference) or row (axial) directions and let N represent the total number of columns and rows in the image. If m_i is the median of the signal from the i^{th} column or row, then the suppressed signal is expressed as

$$s_i = s_i - m_i, \quad i = 1, 2, \cdots, N. \tag{3-5}$$

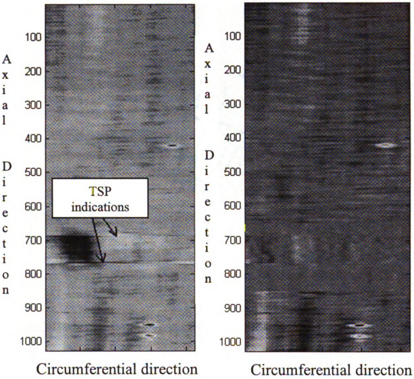

(a) (b)

Figure 3.6 TSP Suppression: (a) vertical component of raw eddy current data at 300 kHz (b) data after TSP suppression

3.2 Band-Pass Filtering, Adaptive Thresholding and ROI Detection

Band-pass filtering is used to remove undesired artifacts and noise signal indications in the eddy current data. First, consider a low-pass filter that attenuates high frequency components of the signal that exists beyond a specified frequency denoted by distance Do from the origin of the centered transform. This two-dimensional ideal low-pass filter has the transfer function

$$S(u,v)=\begin{cases}1 & D(u,v)\le Do\\ 0 & D(u,v)>Do\end{cases} \qquad \text{……….(3.6)}$$

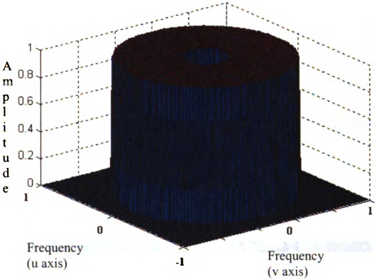

Figure 3.7a Ideal Band Pass Filter

where D_o is a specified non-negative quantity and D(u,v) is the distance from point (u,v) to the origin in the frequency domain . Assuming the synchronized two-dimensional eddy current data is of size M x N, then the centered transform which is also of the same dimension has its origin at (u,v) = (M/2,N/2). As a result, the distance from any point (u,v) to the center (origin) of the Fourier transform is defined as [31]

$$D(u,v)=[(u-M/2)^2+(v-N/2)^2]^{1/2} \qquad \text{……. (3.7a)}$$

A band-pass filter removes or attenuates a band of frequencies about the origin of the Fourier transform. An ideal band-pass filter is given by the expression

$$S(u,v)=\begin{cases}0, & D(u,v)<(Do-\frac{W}{2})\\ 1, & (Do-\frac{W}{2})\le D(u,v)\le (Do+\frac{W}{2})\\ 0, & D(u,v)>(Do+\frac{W}{2})\end{cases}$$

…………………. (3.7b)

where W is the width of the pass-band and D_o is its radial center [31]. Figure 3.7a shows a surface plot of an ideal band pass filter and figure 3.7b shows the performance of band pass filtering on the raw data.

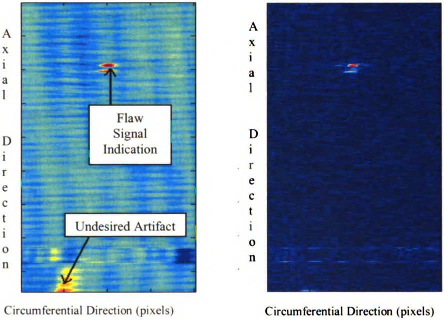

(a) (b)

Figure 3.7b Band pass filtering in the two-dimensional frequency domain. (a) vertical component of raw eddy current data at 300 kHz (b) data after band-pass filtering

Following filtering, a region detection algorithm is used to identify potential locations of flaw signal indications, called the Regions of Interest (ROI). The ROI is obtained using adaptive thresholding. Eddy current data collected from different locations in the tube possess different signal characteristics and hence thresholding schemes have to be adaptive based on the quality of data at hand. One method involves setting an absolute threshold for magnitude and an interval threshold for phase values. In magnitude thresholding procedure, signals whose magnitude is less than the threshold level are treated as noise and set to zero. In phase thresholding or phase gating, signals with phase angles outside a specified interval (flaw plane) are eliminated. In an alternate ROI detection procedure an adaptive thresholding scheme is used to optimally vary the threshold value for different regions in the tube. This scheme computes the histogram of voltage values in a local segment of image. The threshold is then computed as:

$$t = \mu + K\left[\max(V_L) - \min(V_L)\right] \tag{3.8}$$

where, μ = Median of the voltage values in a local (segmented) region of the image

V_L = Set of voltage values that lie in three bins around the median value in the voltage histogram of the local (segmented) region of the image

K = Constant, chosen based on the magnitude of the 20% axial ID defect in the corresponding calibration file

t = Threshold chosen for the local region

A single threshold computed using mean μ and standard deviation σ of the data collected from more than one tube region often yields sub-optimal performance during flaw detection. The variant of the adaptive thresholding scheme computes individual thresholds for data from different tube sections based on their local statistics. The ROI detection scheme can be represented mathematically as follows:

$$x_k^r = \begin{cases} flaw, & |x_k^r| \geq \tau_r \\ noise, & |x_k^r| < \tau_r \end{cases} \tag{3.9}$$

where $\tau_r = \eta.percentile\left(X^r\right)$ is threshold for sample x_k in rth tube region and η is a scalar ranging from 0 to 100. The binary images obtained by thresholding the filtered data is fused by performing a logical intersection of the binary images across frequencies channels. Such data fusion results in high detection rates along with low false call rates. Figure 3.8 and 3.9 shows the performance of band pass filtering on sample data, and ROI detection using adaptive thresholding.

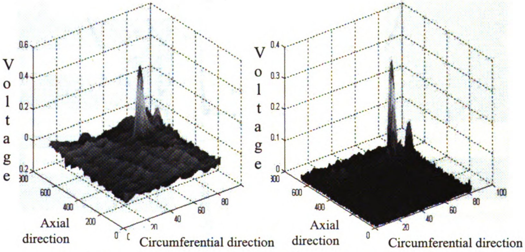

Figure 3.8 TTS suppression using band pass filtering for a tube containing a circumferential defect along the edge of the TTS (a) Original +Pt Circumferential 300 kHz (b) Filtered +Pt Circumferential300 kHz

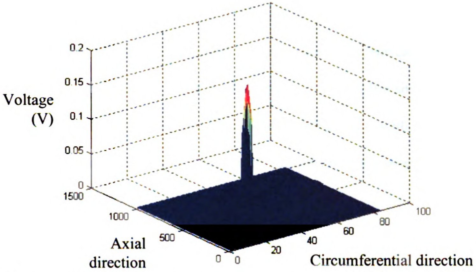

. **Figure 3.9** Thresholding algorithm performance for the tube shown in +Pt Circumferential 300 kHz

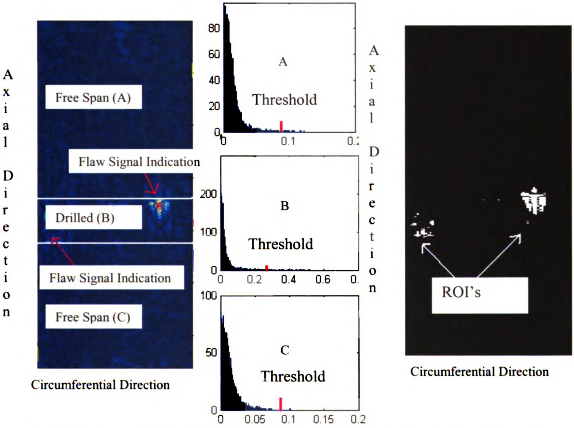

Figure 3.10a ROI detection using region based adaptive thresholding algorithm.

3.3 Classification

After the regions of interest (ROIs) are identified, a classification algorithm is applied to classify each ROI into one of several classes. Figure 3.10a shows the image of vertical component of the thresholded eddy current RPC data with potential defect indications identified after filtering. Each of these indications is processed individually by the classification routines.

The classification module consists of two steps, namely, feature extraction and classification. A feature extraction algorithm is used to extract features from the preprocessed data in the ROI. Features such as maximum magnitude in the ROI and its corresponding phase value are samples of features. The extracted features are subjected to a classification algorithm or rules for discriminating between actual defects and noise. The rule base contains a set of heuristically obtained rules that are that are formed by using predicate logic [6], and are applied sequentially to eliminate false calls, and retain true flaw indications. For example, let the maximum magnitude (vertical 300 kHz axial channel) in a region of interest be denoted as **M**. Furthermore, let the corresponding phase values across 300 kHz, 200 kHz and 100 kHz axial channel be denoted as $\mathbf{P_3}$, $\mathbf{P_2}$ and $\mathbf{P_1}$ respectively. Then the following rules apply for calibrated flaw data:

1. Outer diameter (OD) axial flaw:
    - $\mathbf{P_3} \geq 35$, $\mathbf{P_2} \geq 35$, $\mathbf{P_1} \geq 35$ (defines flaw plane for OD defects)
    - $\mathbf{P_3} \leq 180$, $\mathbf{P_2} \leq 180$, $\mathbf{P_1} \leq 180$ (defines flaw plane for OD defects)
    - $\mathbf{P_3} \geq \mathbf{P_2} \geq \mathbf{P_1}$ (defines order in flaw plane)

2. Inner diameter (ID) axial flaw:
   - $\mathbf{P_3} \geq 0$, $\mathbf{P_2} \geq 0$, $\mathbf{P_1} \geq 0$ (defines flaw plane for ID defects)
   - $\mathbf{P_3} < 35$, $\mathbf{P_2} < 35$, $\mathbf{P_1} < 35$ (defines flaw plane for ID defects)
   - $\mathbf{P_3} \geq \mathbf{P_2} \geq \mathbf{P_1}$ (defines order in flaw plane)
3. Maximum magnitude in ROI, $\mathbf{m} \geq \mathbf{M}$

Figure 3.10b shows an illustration of ROI classification using the rule bases. M is typically obtained by identifying a conservative lower bound above which the magnitudes of flaw signal indications in the training data are greater.

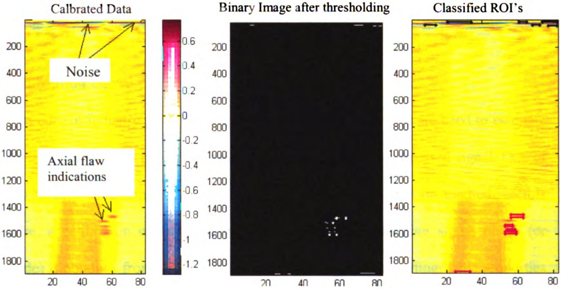

Figure 3.10b ROI classification for axial flaw indications and noise using rule-bases. The magenta and black rectangles in (c) correspond to classified axial flaws and noise respectively

3.4 Defect Characterization

Defect characterization is the estimation of the depth profile of the detected defect ROIs. Several factors contribute to distortion of the measured eddy current signal. One example is the limitation of the resolution of inspection system relative to the flaw length. In other words, the resolution of the horizontal eddy current scans in a two-dimensional

ROI must be significantly larger than the length of the crack in order to obtain a depth profile at each horizontal slice. Another factor is that the probe speed changes during the inspection process which introduces errors in the collected data. Additive noise generated during the scan due to the presence of contaminants and surface roughness can also introduce noise. Furthermore, when an analog signal is sampled to generate a digital signal, quantization errors are introduced. This can lead to additional distortion of the signal. All these issues make defect characterization in steam generator tubes a very challenging task. The different contemporary characterization algorithms implemented for defect profiling are explained in this section [24].

3.4.1 Calibration Curve

In current industry practice, simple characterization schemes are used to estimate the flaw length and depth profile for each flaw indication in the processed signal. One of the most widely used approaches for sizing defects is the calibration method. In this procedure, a calibration curve relating flaw depth to corresponding signal phase (or magnitude) is obtained from the calibration specimen of similar metallographic properties and physical dimension as the test specimen. For a given defect signal, its equivalent depth is predicted using simple interpolation methods. For example, we assume that the calibration curve *f* is piece-wise linear between each of the known mapping points. The phase and magnitude computed from flaws in the calibration standard tube are used to construct the function *f*. Figure 3.11 and 3.12 shows typical phase and magnitude calibration curves respectively.

During inspection, for a given defect signal, the relationship used to predict the defect depth when the signal phase is b is given by [3.10]:

$$f(b) = f(a) + \frac{b-a}{c-a}\left[f(c) - f(a)\right] \qquad \text{.................. (3.10)}$$

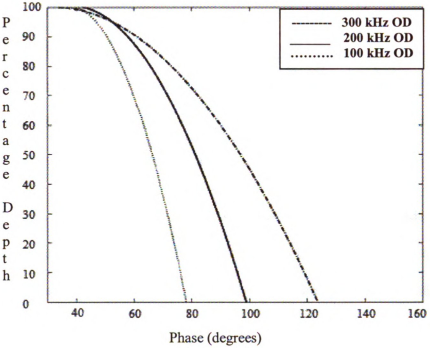

Figure 3.11(a) Phase calibration curves

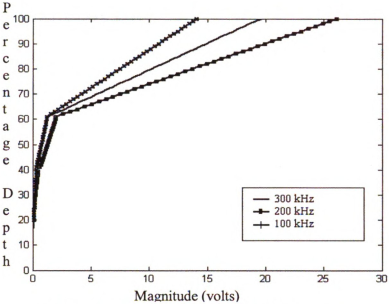

Figure 3.12 (b) Magnitude calibration curves

The defects impressed on the calibrating specimen are man-made and have dimension that are untypical of cracks due to corrosion or inter granular attack that occur naturally in the tube during the normal operation of the steam generator. Artificial flaws created for the purpose of calibration usually give a higher signal response as compared to naturally occurring cracks having the same maximum depth. This is because naturally occurring cracks are thinner and finer in width than calibrating notches. As a result, the thinner a 100% TW crack as compared to the 100% TW calibration notch, the more it falls short of the 20V magnitude and 35° phase standards after calibration. It is therefore common to see 100% TW cracks with a phase between 50° - 66° and magnitudes of about 4V. For this reason, the calibration method is inherently flawed and cannot accurately characterize flaws.

3.4.2 Enhanced Calibration Curve

An alternative approach which may yield better characterization results is to fit a curve to the data of magnitude and corresponding maximum depth values obtained from training flaws. The magnitude and maximum depth coordinates are plotted and the curve is fitted in a least square sense to the scatter plot. This curve can be represented by the general expression:

$$\log_e(flaw_{depth}) = a_0 + a_1 \log_e(flaw_{magnitude}) \quad \ldots\ldots\ldots\ldots\ldots \quad (3.11)$$

The coefficients a_0 and a_1 are empirically determined from the available data set. Figure 3.13 shows a magnitude calibration curve constructed using the logarithmic mapping. The resultant curve again serves as the calibration curve.

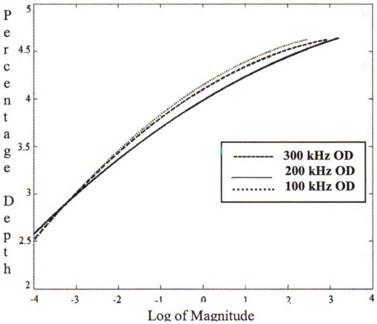

Fig 3.13 Magnitude calibration curve using equation (5)

3.4.3 Model Based Profiling

Another approach for defect profiling is the use of numerical models [33] in an iterative framework. An application of this method lies in the use of a computational model, such as the finite element model [34]. The underlying idea of this approach is illustrated in the schematic diagram shown in figure 3.14. It starts with an initial estimate of the defect profile parameters and solves the corresponding forward problem to determine the corresponding signal. The error between the estimated and measured signals, F, is minimized by updating the defect profile iteratively. However, this method tends to be computationally expensive as it requires execution of a 3D FE model in each iteration to achieve the desired profile.

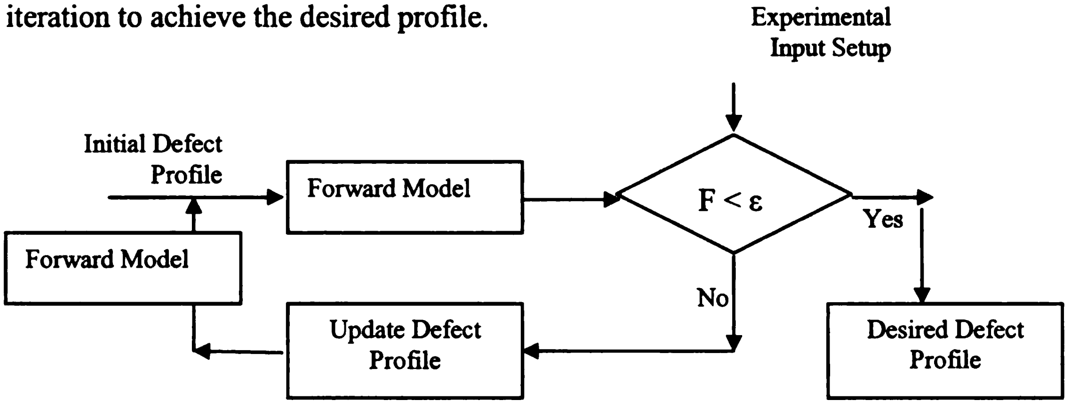

Figure 3.14 Iterative inversion method for solving inverse problems

This thesis aims to investigate a more sophisticated approach for flaw characterization which employs the use of a trained radial basis function for mapping magnitude and phase values utilizing data at all available frequency obtained from the plus-point coil onto an estimated depth value. Mathematically, this approach provides a nonlinear mapping from an input vector (signal feature) space on to an output vector (defect depth profile) space. The next chapter introduces the underlying concepts of the radial basis function neural network (RBFNN). A proposed flaw length estimation technique is also explained.

CHAPTER 4 Artificial Neural Networks

4.1 A Little Biology

The human brain consists of a specialized network of billions of highly interconnected cells called neurons (see figure 4.1). Each cell receives electrical signals from as many as 10,000 other cells and transmits or inhibits an output signal based upon the input signal pattern [10]. Although modern science may not have an exhaustive knowledge about the mechanism and functionality of the human brain, it is possible to mimic some of its abilities such as learning, pattern recognition and generalization.

The biological neuron consists of four main parts: the body, the incoming channels, the outgoing channel(s), and the connection points between neurons, which are called synapses. In other words, the synapses are the gateway for neuron-to-neuron signal transmission. A neuron receives many signals from other neurons at the synapses in which some processing occurs before the signals are sent down the incoming channel to the neuron body. This signal processing is basically achieved by weighing each incoming signal with the result that each of these signals has a different excitation effect on the neuron. As such, the synapse is traditionally an amplifier or attenuator of input signals, which in turn have a stronger or weaker effect on the receiving neuron. A highly excited neuron sends out an output signal while an inhibited one does not (see figure 4.2).

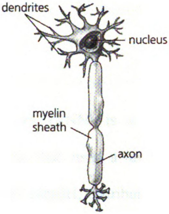

Figure 4.1 The neuron [16]

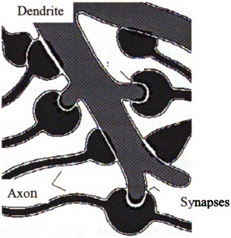

Figure 4.2 Synaptic connections with a neuron [17]

The primary function of the neuron body is to combine all the incoming signals and determine if the total is enough to send out a signal. In other words, a comparison with an activation threshold is the decisive criterion for transmitting or inhibiting an output signal. Learning occurs in the brain in the form of changes to the synaptic weights [10]. There are a few theories which have been developed to explain how the learning process works. The general opinion is that synapses change over time as signals are received, and this constitutes learning. Knowledge is captured in bits and pieces by the weights synapses attach to the incoming signals. As a result, knowledge is spread out across many neural connections.

4.2 Artificial Neural Network

An **artificial neural network** (ANN) is a densely interconnected group of computational nodes or neurons that uses a mathematical model for processing information. ANN is a massively parallel, distributed processor with the capability to store and retrieve experiential knowledge [8]. The characteristics of the network are determined by the nature of the processing elements, and strengths of the interconnections, known as synaptic weights, which are used to store the knowledge. The network acquires knowledge by a learning process, which modifies the synaptic weights in an orderly fashion to achieve a desired objective. The basic neuron model is the single layer perceptron which accepts an n-dimensional vector and performs a weighted sum, adds a bias and passes the result through a nonlinear function to yield an output. The primary use of a perceptron is in pattern classification. Patterns are distinct features that are derived from signals of different classes. The single layer perceptron can discriminate between two classes by separating them with a linear decision boundary in the feature space. The perceptron model cannot generate nonlinear decision boundaries and as a result cannot be used in most real world pattern recognition problems, wherein classes are not linearly separable [8]. A multilayer perceptron network overcomes this limitation and can generate highly nonlinear decision boundaries for classification problems.

4.3 Neurons

Biological and artificial neural networks alike contain neurons which are interconnected in order to transfer information from a source to a destination. The knowledge of a network does not reside solely in a specific part of the network but is distributed across the interconnections between the neurons. Every neuron computes its own output by finding a weighted combination of the input signals, generating an activation level and transmitting that to an output or a transfer function. The collection of weights arranged in rows and columns is called the weight matrix.

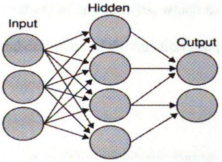

Figure 4.3 A simple neural network showing connected nodes [18]

4.4 Layers

A neural network consists of neurons connected to each other in layers. The configuration of the layer structure plays an important role when building a neural network to achieve a desired goal. Some of these neurons are in direct contact with the outside world and are usually responsible for directly receiving external stimuli from a source or delivering directly to a final destination point. However, some neurons communicate with other neurons are called the hidden neurons.

The architectural layout of the basic neural network, as shown in figure 4.3, contains the input layer, the hidden layer and the output layer. External stimuli from the outside world, such as a continuous or digital electrical signal, temperature, pressure or light energy, are fed into the network by the input layers. The received information is sent to the hidden layer neurons which lie between the input and output layers. The hidden layer forms a complex network of neural components that project the neural network's solution to the problem. The output neurons further process information obtained from the hidden neurons. The output information at this point is the neural network's response to the input information [10]. A variety of neural network architectures and learning algorithms have been developed to address a variety of applications, which mainly differ from each other in the network architecture and definition of the function computed at each node.

4.5 Radial Basis Functions

Radial basis functions are radially symmetric functions for which the response decreases monotonically with distance from a central reference point. A special class of radial functions is the Gaussian which is defined mathematically by

$$h(x) = \exp\left(-\frac{(x-c)^2}{r^2}\right) \qquad \text{..................} (4.1)$$

where **x** is the input vector, **c** is the position vector of the basis centre in the multi-dimensional space and **r** is its standard deviation (see figure 4.4).

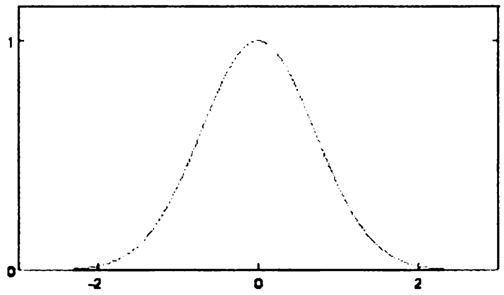

Figure 4.4 Gaussian with **c** = 0 and **r** = 1

4.6 Radial Basis Function Neural Networks

A radial basis function (RBF) is a powerful tool for interpolation in multi-dimensional space. The architecture of RBF networks, in its most basic form, involves three layers as shown in Figure 4.3: an input layer of source nodes, a single hidden layer which operates as a kernel node, and an output layer. The nodes in the hidden layer are characterized by a set of basis functions, typically a Gaussian basis function. The centers of the basis functions are determined from a scatter plot of variables by using a clustering algorithm. The spread (standard deviation) of the basis functions are proportional to the cluster size. The objective of the network is to determine an input-output mapping function using the training data. The mapping function determined by the output interconnection weights is determined by a matrix inversion step (assuming matrix is invertible). The mapping estimated provides the best fit to the data in a statistical sense. The mapping is accomplished in two stages. First, a nonlinear transformation connecting the input layer to the hidden layer is defined by a set of radial basis functions. A linear transformation is then performed between the hidden layer and output layer. Subsequently, an interpolation is performed during a generalization process with unknown data [20]. In contrast to statistical analysis where approximations are performed on complete data sets, RBF's use a subset of data with the aim of estimating the characteristics of data outside the subset by interpolation techniques.

Suppose we want to approximate a real valued function **f(x)** by **s(x)** given the set of values $f = (f_1, \ldots\ldots, f_n)$ corresponding to the real-valued input points $x = \{x_1, \ldots\ldots, x_n\}$, then an expression for **s(x)** using RBF's is given in equation (4.2) where **p(x)** is a polynomial,

$$s(x) = p(x) + \sum_{i=1}^{N} \lambda_i \Phi(|x - x_i|) \quad \ldots\ldots\ldots\ldots\ldots (4.2)$$

λ_i is a real-valued weight, | * | represents the Euclidean norm, ϕ is the basis function and $|x - x_i|$ is a measure of the distance between x and the basis center x_i. Proper training of the network requires optimization of the weight parameters which is critical to reducing the error between f(x) and s(x). A simple training algorithm to achieve this stems from the gradient descent approach. Gradient descent is based on the observation that if the real-valued objective function **H(w)** is defined and differentiable in a neighborhood of a point **a**, then **H(w)** decreases *fastest* if one goes from **a** in the direction of the negative gradient of **H(w)** at **a** (i.e. along **-ΔH(w)**) [19]. It follows that, if

$$\mathbf{b} = \mathbf{a} - \gamma\,[-\Delta \mathbf{H}\,(\mathbf{w})] \quad \ldots\ldots\ldots\ldots\ldots\ldots (4.3)$$

for $\gamma > 0$ a small enough number, then $\mathbf{H(a)} \geq \mathbf{H(b)}$. With this observation in mind, one starts with a guess $\mathbf{w_o}$ for a local minimum of $\mathbf{H(w)}$, and considers the sequence $\mathbf{w_o}$, $\mathbf{w_1}, \mathbf{w_2}$ ...such that

$$w(t+1) = w(t) - \gamma[-\Delta H(w)] \qquad \text{.....................} \ (4.4)$$

We then have $\mathbf{H(w_o)} \geq \mathbf{H(w_1)} \geq \mathbf{H(w_2)}$ . . .. and the sequence $\mathbf{w_t}$ converges to the desired local minimum. In particular, gradient descent training requires that the weights be adjusted at each time step by moving them in a direction opposite from the gradient of the objective function [19].

4.7 Depth Profiling Using RBFNN

In the proposed depth profiling algorithm using RBFNN, there are two major steps. The first step is to estimate the length of the defect and the second step is depth profile along the length of the defect. Length is typically defined along the axial direction for axial cracks and along the circumferential direction for circumferential cracks.

4.7.1 Length Estimation

The ROI selected by an analyst typically contains a region around the defect. Due to the presence of additive white and colored noise in the eddy current data, it is essential to accurately discriminate between noise and true defect indications in the measured signal for the purpose of depth profiling. Setting a magnitude threshold and/ or a phase interval are two possible strategies towards this goal. However, the efficacy of this approach is compromised when eddy current data of low signal to noise ratio is analyzed. From empirical studies, the magnitude thresholding and phase windowing method produces satisfactory flaw length estimates when the signal to noise ratio is high and defect depth value is over 30% TW. Flaw length estimation techniques employed in this research relies on an adaptive threshold scheme based on the statistical properties of the synchronized calibrated two-dimensional eddy current signal in the region on interest (ROI).

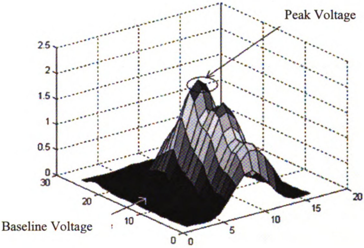

Figure 4.5 Calibrated flaw magnitude distribution (in volts) showing base-line and peak voltage inside region of interest

In order to define the parameters required for the proposed flaw length estimation technique, consider the surface plot of the ROI in figure 4.5. The ratio, γ, of the maximum signal magnitude and the base-line magnitude inside the ROI (see figure 4.5) follows an empirical relationship with the optimum magnitude (η) threshold given by

$$\eta = \alpha \exp\{-\lambda[\gamma - \gamma_0]\}\ \% \qquad \text{..................} \ (4.5)$$

where the constants α, λ and γ_0 are determined empirically from the available profiling data such as shown in figure 4.6. The curve in figure 4.6 was obtained by finding the coefficients of a piece-wise polynomial that fits the scatter plot in a least-squares sense as given in equation (4.6). From the piece-wise curve fit, α, λ and γ_0 can be determined.

$$\text{Threshold} = \begin{cases} 10{*}\exp[-0.0151{*}(\gamma - 1)], & \gamma \leq 152 \\ 1.0, \text{ otherwise} \end{cases} \qquad (4.6)$$

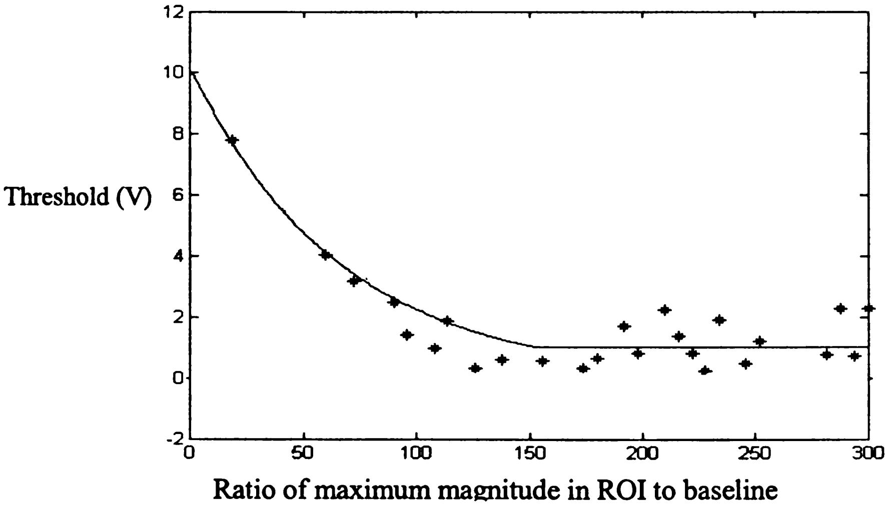

Figure 4.6 Empirical relationships between optimum thresholds and ratio of peak to base line voltages in ROI

The flaw length is estimated by multiplying the number of horizontal slices that contain magnitudes greater than the threshold with the axial scale (length units per horizontal slice) to yield the flaw length in inches. A sample flaw length estimation process is shown in figure 4.7. The number of horizontal slices having magnitudes greater than the computed threshold is averaged across frequency channels.

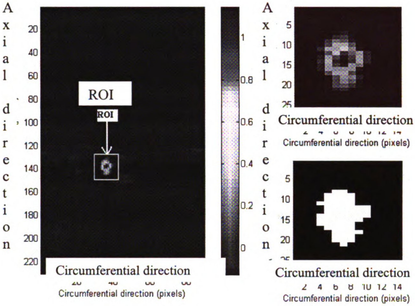

Figure 4.7 Length estimation scheme. Left: vertical component of raw eddy current data at 300 kHz with ROI indicated. Top right: Magnitude distribution in ROI with 29 horizontal slices. Bottom right: Binary image of thresholded ROI. Axial span of the effective ROI (corresponding to white pixels) ranges from the 8th to the 22nd horizontal slice making a total of 15 slices. Estimated length of defect equals 15 multiplied by the axial scale (length units per horizontal line scan)

Current thresholding schemes employ statistical variance of data within the region of interest for threshold computation. Typical threshold levels are set at 2 or 3 times the standard deviation. However, this scheme becomes flawed if the dimension of region of interest is not fixed. In the event that the ROI is selected manually in a semi-automated length estimation scheme, the standard deviation of the signal magnitude within the ROI becomes dependent on the selected ROI size and, in turn, affects the flaw length estimate. This process poses a poor repeatability strategy. On the other hand, the proposed method offers better repeatability as the maximum magnitude in the ROI is a constant. The baseline voltage, however, can be made independent of ROI size by applying a two dimensional median filtering operation in the signal pre-processing stage. Therefore, the computation for γ in equation 4.5 is a constant irrespective of the ROI size and, in turn, yields a constant threshold. Figure 4.8 and 4.9 shows the effect of varying the size of the ROI engulfing a defect signal indication using the conventional and proposed methods respectively. In the proposed length estimation procedure, the number of horizontal slices having magnitudes greater than the computed threshold is 13 in all four ROI's selected. In contrast, the lengths estimated by choosing the magnitude threshold to be twice the standard deviation in the different ROIs are 11, 12, 12 and 13 in the order of increasing ROI size.

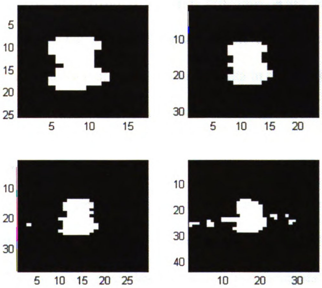

4.8 Effect of varying ROI size on length estimation using twice the standard deviation in ROI as threshold

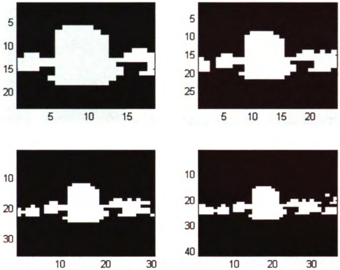

4.9 Effect of varying ROI size on length estimation using proposed length estimation scheme

4.7.2 Depth Profiling

The second step in defect characterization is depth profiling. After length estimation process is completed, eddy current signals lying within the defect are used for defect depth profiling. Each horizontal slice of the eddy current data in the 2D ROI is mapped to a single depth value using a trained RBF neural network.

4.8 Training the Network

In order to optimize network performance, the network is trained using eddy current data from laboratory-simulated flaws with the corresponding metallographic depth profiles (MET). The training data provides consistent and accurate correspondence between the measured magnitude or phase values and the depth values obtained from metallographic examination. The regions of interests in the synchronized and calibrated eddy current data are broken down into horizontal slices as shown in figure 4.8.

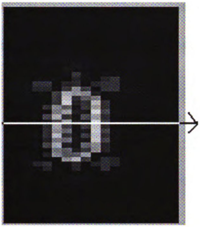

Figure 4.10 ROI showing arbitrary feature vector structure

From each horizontal slice, the maximum absolute magnitude and its corresponding phase value is computed across all available frequencies in the Plus-Point axial channel. This feature vector arrangement is depicted in figure 4.8 where feature vector at slice *i*

$$\mathbf{X}_i = [M_{300}\ M_{200}\ M_{100}\ P_{300}\ P_{200}\ P_{100}] \qquad (4.7)$$

where M_{300}, M_{200} and M_{100} represent the maximum magnitude per horizontal slice across 300 kHz, 200 kHz and 100 kHz respectively; P_{300}, P_{200} and P_{100} represent the corresponding phase value across 300 kHz, 200 kHz and 100 kHz respectively. The phase in this context refers to the difference between 180° and the arctangent of the ratio of the vertical amplitude to the horizontal amplitude both corresponding to the location of the maximum magnitude in the horizontal slice in question. In other words, if a pair of corresponding horizontal slices – N elements in length – in the vertical and horizontal channels are denoted V and H, then the magnitude vector, M, is computed as

$$M = \sqrt{V^2 + H^2} \qquad \ldots\ldots\ldots\ (4.8)$$

Assuming the maximum absolute value in M, denoted as m, corresponds to the xth element in the slice, then the phase, P, is computed as

$$P = 180^\circ - \arctan(\frac{V[x]}{H[x]}) \qquad \text{..........} \ (4.9)$$

In this research work three magnitude and three phase values obtained at 300 kHz, 200 kHz and 100 kHz make up the feature vector for training.

The corresponding MET result for each region of interest is sampled or interpolated so as to make the number of sample points consistent with the number of horizontal slices in the region of interest in question. Figure 4.9 shows a sample MET result and the resized version to be used for training the network. This resizing procedure can be defined mathematically by the following procedure

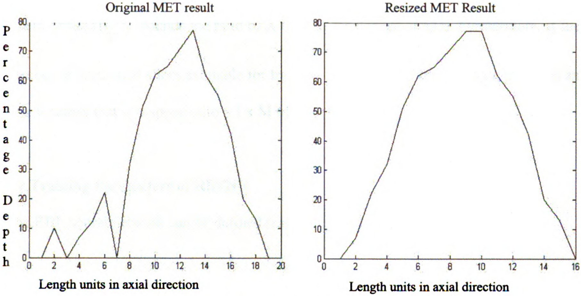

Figure 4.11 Original and modified MET result

- Let the number of sample points in the original MET be X and let the number of horizontal slices for flaw length estimation (obtain by thresholding the ROI) be Y.

Then the length units for the modified MET will be sample points with ascending values 0, (Y/X), 2 x (Y/X), 3 x (Y/X)... Y.

- Assuming N*D*, *OD*, *NL* and *OL* are the modified depth vector, original depth vector, modified length vector and old length vector respectively The corresponding depth values for the modified MET result is given by

$$ND(i) = \frac{[(OD(round(\frac{X}{Y})*(i+1)) - OD(round(\frac{X}{Y})*i)*(NL(i) - OL(round(\frac{X}{Y})*i)]}{OL(round(\frac{X}{Y})*(i+1)) - OL(round(\frac{X}{Y})*i)} - OD(round(\frac{X}{Y})*i)$$

(4.10)

i = 1, 2 ....Y-1;

where "$round(\frac{X}{Y})$" rounds the ratio of X to Y to the nearest integer. Furthermore, if the number of horizontal slices available for training is M, then the input feature matrix is an M x 6 matrix that is mapped onto a 1 x M MET result array.

4.9 Training Parameters of RBFNN

The RBF neural network can be defined mathematically as [22]

$$y = \sum_{i=1}^{i=P} w_i f(\| x - t_i \|, \sigma_i) + w_o \quad \ldots\ldots. (4.9a)$$

where x is the input vector in $\boldsymbol{R}^N$ and y is the output vector in $\boldsymbol{R}^M$. The hidden layer of RBFNN consists of $\boldsymbol{P}$ centers of radial basis functions denoted as $\mathbf{t}_i$, i = 1,..., P. f *is* a scalar valued radial basis function and the scalar quantity σ is the spread or radius of the i^{th} center, t_i. w_i is the weight vector corresponding to the i^{th} center.

The training of the RBFNN involves estimating the parameters w_i, t_i and σ_i (collectively denoted as Θ) from the available training data. Θ is defined as

$$\Theta = \{(w_i, t_i, \sigma_i) \mid i = 1, \ldots, n\} \quad \ldots 4.9b$$

The mapping of RBFNN can be compactly represented using the notation, $\tilde{y}_i = f(x_i, \Theta)$.The objective of training is to minimize the squared error between the predicted values and true values of y_i's and can be denoted as [22],

$$\Theta : \min_{\Delta} \{\| y_i - f(x_i, \Theta) \|^2\} \qquad (4.10)$$

The minimization problem is typically highly ill conditioned and the solution is regularized for each parameter separately using suitable constraints. Following sections review training algorithms for estimating each parameter.

4.9.1 Selection of Centers of Basis Functions (t_i) [22]

This involves the optimal computation of centers in training data clusters. Since the class information is unknown prior to training the RBFNN, unsupervised clustering approaches are used. The unsupervised clustering can be performed using number of approaches but the K-means clustering approach is deployed in this research. K-means clustering is extremely intuitive and simple algorithm and produces near optimal results in most cases. However, it is sensitive to the starting point of the operation and incorrect selection of starting point may result into bad clustering performance [22]. An Iterative Self-

Organizing Data Analysis Techniques (ISODATA) clustering process as described in [22] is an enhanced version of K-means clustering.

4.9.2 Selection of Spreads or Radii of the Centers (σ_i) [22]

The determination of spread of each center can be done using the Iterative Self-Organizing Data Analysis Techniques (ISODATA) algorithm described in [22]. This algorithm computes the two critical properties that are useful in determining the spread, which are: (1) Inter-cluster distances (γ_i's) and (2) Intra-cluster distances (s_i's).

The γ_i's and s_i's are defined as [22],

$$\gamma_i = \min\{\| t_i - t_j \|, j = 1,\ldots,P; j \neq i\}, i = 1,\ldots,P$$
$$s_i = \max\{\| x_j - t_i \|, j = i,\ldots,P\}, i = 1,\ldots,P \qquad \ldots\ldots\ldots\ldots(4.12)$$

γ_i's give information about the distance of the nearest neighboring cluster. When the spread of a center is based on this parameter, the basis function covers the entire space between all the neighboring clusters thereby providing a complete mapping of the input space covered by the training data.

4.9.3 Computation of Weights (w_i) [22]

In order to estimate the weights, the input feature matrix and the output MET results must be known. Let the number of training samples be *M*. The input training data can be represented in the form of a matrix X of dimensions *M* x *6* and output data can be represented by a matrix Y of dimensions *M* x *1*. As described in [22], using the input data, a radial power basis function, centers and their spreads the matrix of basis function can be computed as,

$$F(i,j) = (\| x_i - t_j \|^2 + 1)^{-\frac{1}{\sigma_j^2}}, i = 1,\ldots, n; j = 1,\ldots, P \quad \ldots \qquad (4.13)$$

F has dimensions *6* x *P*. The RBFNN equation in matrix form can then be written as,

$$FW = Y \qquad (4.14)$$

The weight matrix W of dimensions *P* x *M* can be computed using the pseudo inverse of matrix F and output matrix Y. However, direct use of pseudo inverse in an ill conditioned problem results in an impractical solution. Hence there is need for using a regularization procedure. The solution of equation 4.14 can be regularized using Landweber-Fridman [27] type iterative algorithm. The details of this regularization scheme can be found in [22]. This method is computationally quite efficient and also provides good regularization performance. This scheme is used throughout this thesis. The next chapter describes the experimental analysis and results for depth profiling using the calibration curves and the RBF neural network.

CHAPTER 5 Experimental Analysis and Results

5.1 Introduction

In this chapter, two variants of depth profiling schemes using the RBF neural network are described. The first, referred to a RBF1, is implemented by mapping a six-dimensional feature vector comprising three magnitude and three phase values (as described in chapter 4) onto its corresponding a scalar depth value determined from metallographic analysis. The second variant of the RBF approach, referred to RBF2, maps the six dimensional feature vector onto a three dimensional output vector consisting of a consecutive sequence of 3 depth values obtained from metallographic results. The rationale for RBF2 is that knowledge of the depth information in the neighborhood of an arbitrary horizontal slice may contribute to improve the depth estimation corresponding to the same arbitrary slice. The performance of both methods is compared alongside the results obtained from calibration curves. Figure 5.1 shows a schematic of the overall implementation of the depth profiling procedure using the RBFNN.

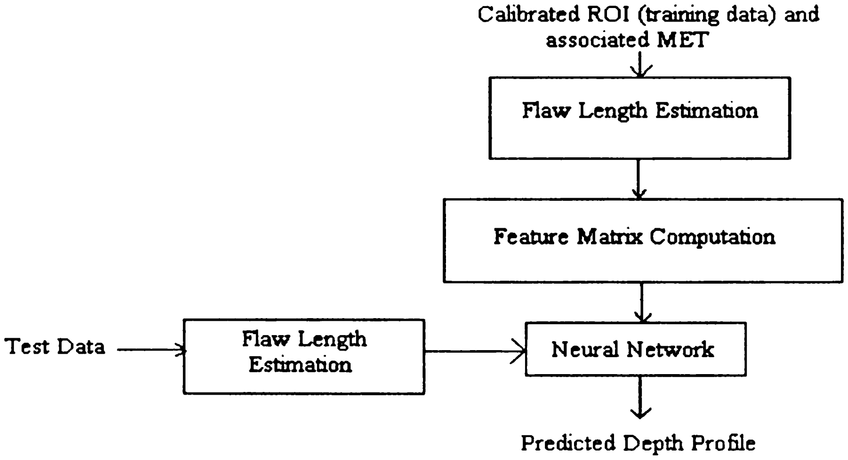

Figure 5.1 Schematic of the overall approach using RBFNN

5.2 Experimental Methodology

Using the length estimation procedure described in Chapter 4, a subset of the total number of horizontal slices in the ROI is first obtained. This subset corresponds to the horizontal slices vectors for which the maximum magnitude along its individual length are equal or above the predetermined voltage threshold given by equation (4.5). By multiplying the number of horizontal slices in this subset with the axial scale – given in length units per slice – length of the flaw in inches is determined.

The peak magnitude and phase at multiple frequencies for each horizontal slice is computed and entered in a feature matrix for training the network alongside the corresponding MET depths values. A general mathematical representation for the RBF1 framework is given as

$$D(j) = RBF1[X(j)] \qquad (5.1)$$

for **X**= [M_{300} M_{200} M_{100} P_{300} P_{200} P_{100}] as defined in section 4.8, j is the current observation; F and D denotes the feature vector and corresponding depth estimate respectively; M_{100}, M_{200}, *and* M_{300} are the magnitude values computed at 100 kHz, 200 kHz and 300 kHz respectively; P_{100} P_{200} P_{300} are the phase values computed at 100 kHz, 200 kHz and 300 kHz respectively. For the RBF2 network, the general representation using similar notation is given as

$$D(j) = RBF2[F(j-1), F(j), F(j+1)] \qquad (5.2)$$

Figures 5.2 – 5.7 show the scatter plot of features magnitude and phase values obtained from the training data at 300 kHz, 200 kHz and 100 kHz against the corresponding depth from metallographic result. From inspection of Figs. 5.2, 5.4 and 5.6 it is apparent that there exist some correlation between magnitude values and flaw depth. Similarly, by inspection of Figs. 5.3, 5.5 and 5.7 it is evident that there exists some correlation between phase values approximately ranging between 35 and 180 degrees and flaw depth at all frequencies. This relationship is expected as the flaws analyzed in this research work are outer diameter axial flaws.

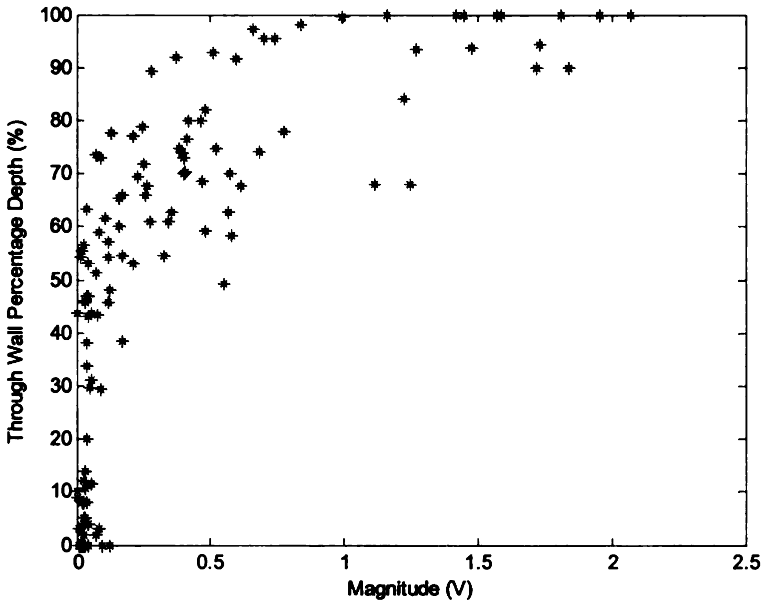

Figure 5.2 Scatter plot of magnitude vs. depth for training sample at 300 kHz

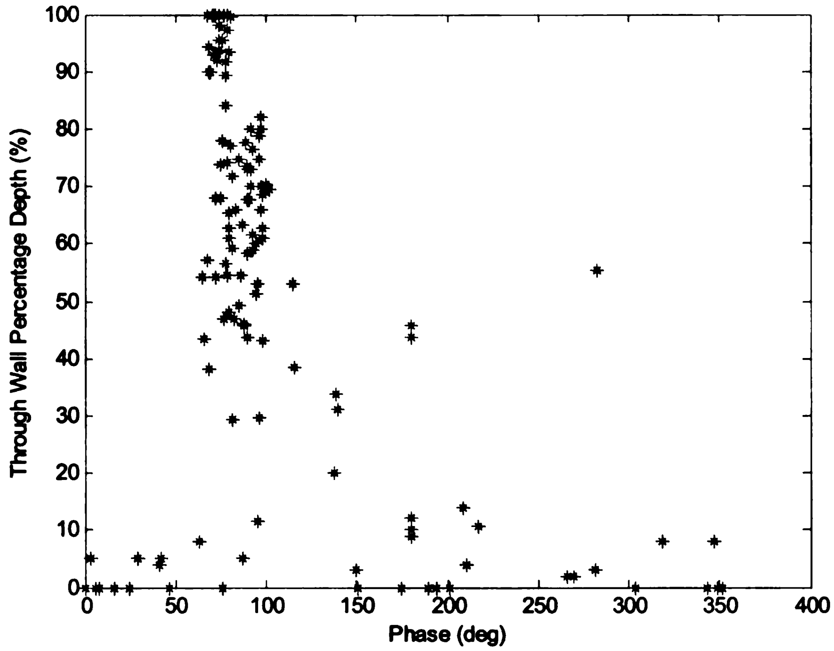

Figure 5.3 Scatter plot of phase vs. depth for training sample at 300 kHz

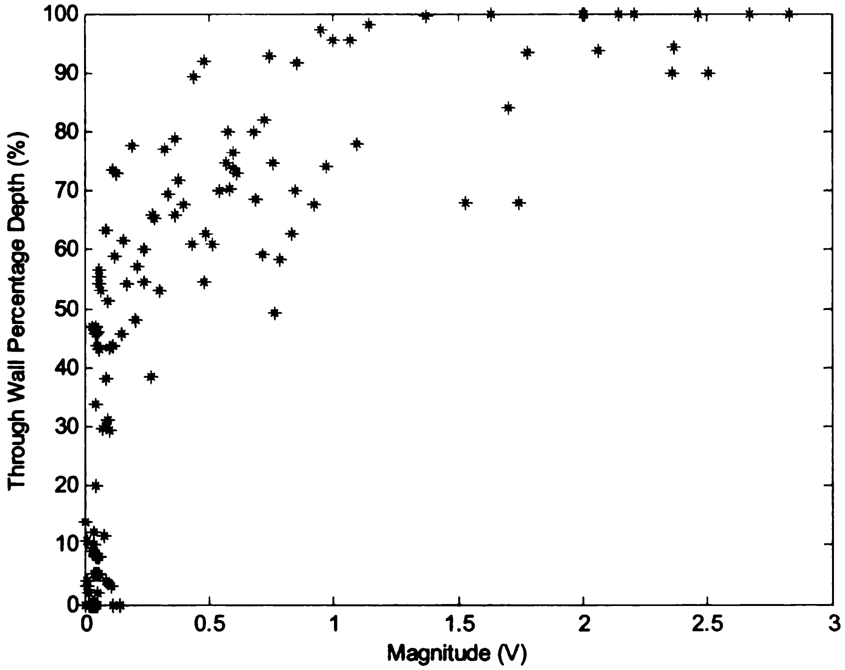

Figure 5.4 Scatter plot of magnitude vs. depth for training sample at 200 kHz

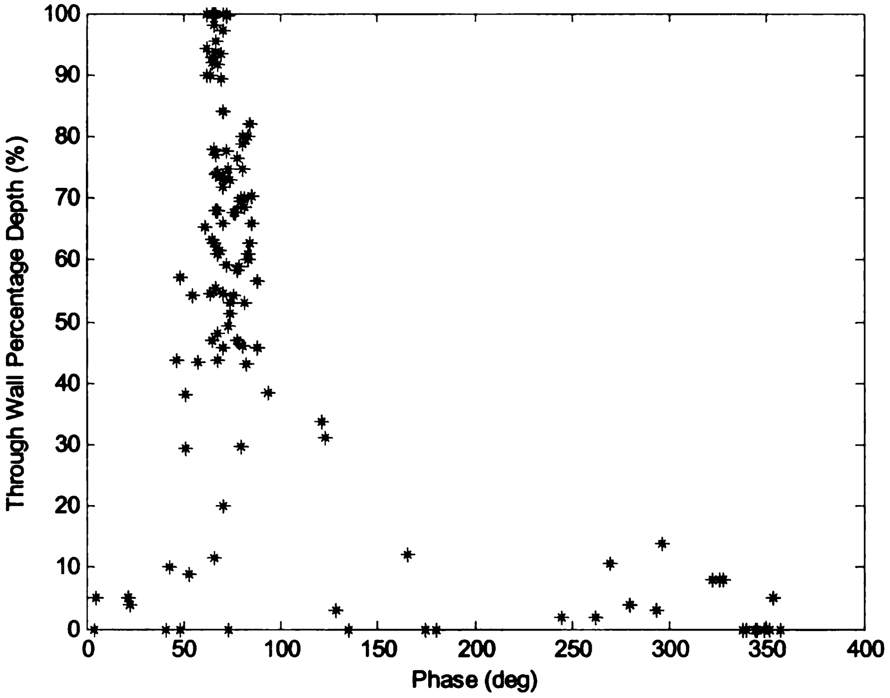

Figure 5.5 Scatter plot of phase vs. depth for training sample at 200 kHz

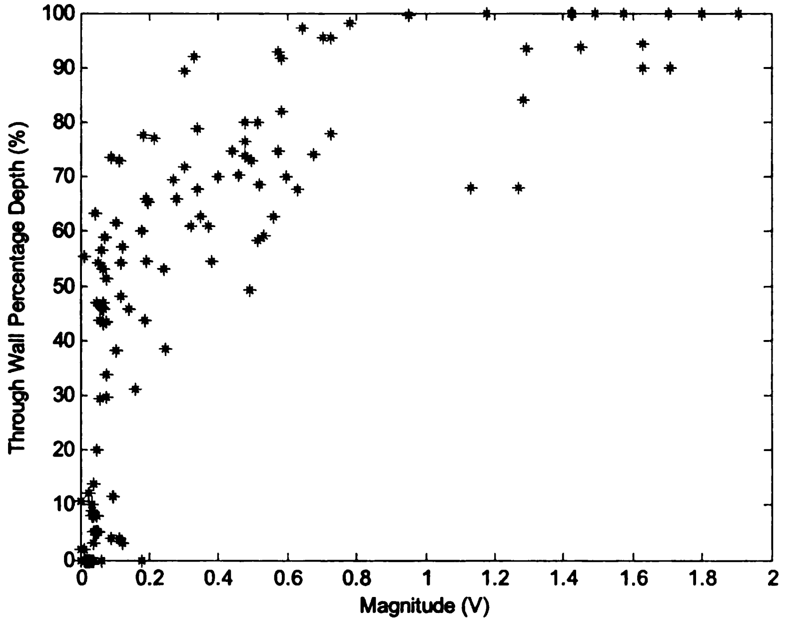

Figure 5.6 Scatter plot of magnitude vs. depth for training sample at 100 kHz

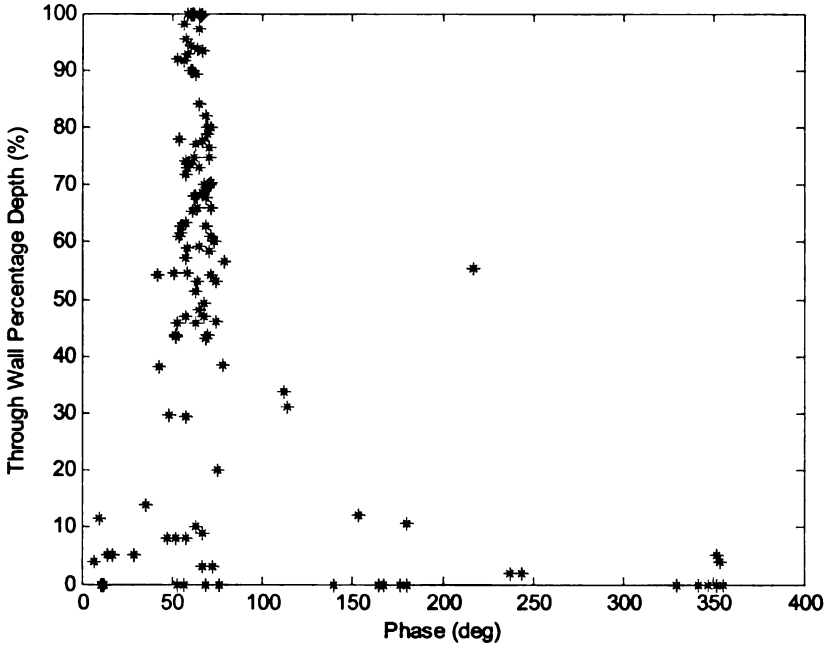

Figure 5.7 Scatter plot of phase vs. depth for training sample at 100 kHz

After defect length estimation, horizontal slices that contain magnitudes greater than the threshold are used to compute the feature matrix and applied to train the RBFNN as described in previous section [22]. The centers of the basis function are computed using the Iterative Self-Organizing Data Analysis Techniques (ISODATA) algorithm, the radii are computed using intra-cluster distance and the weights are computed using the method of regularization described in Chapter 4. A power basis function is used in the hidden layer nodes. The power function is defined in equation (5.3)

$$f_P(\| x - t_i \|), \sigma_i) = (\| x - t_i \|^2 + 1)^{\frac{-1}{\sigma_i^2}} \quad (5.3)$$

The overall training data is randomly divided into training set and test set. Roughly 70% of the data is used for training and the remaining 30% is used for testing. Figure 5.8(a)-

(c) shows the profiling results obtained for three flaws – whose depth profiles have been predetermined using metallographic techniques – using the classical magnitude calibration curve approach (CC), log magnitude curve and the two RBF neural networks, RBF1 (one feature vector per depth) and RBF2 (three feature vector per depth). These flaws were randomly selected from a database of similar flaws whose depth profiles have been experimentally determined by metallographic analysis. This database is generally referred to as the Examination Technique Specification Sheet (ETSS).

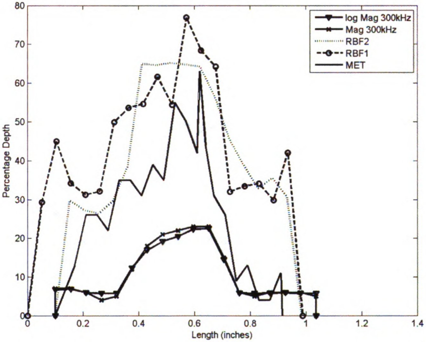

(a)

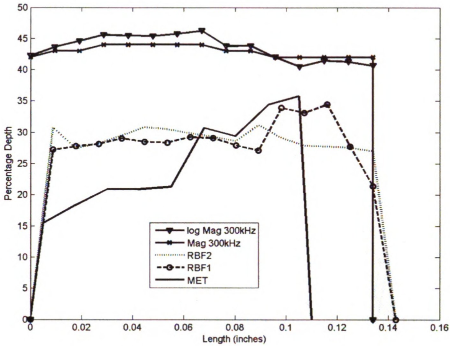

Percentage Depth
Length (inches)
0
5
10
15
20
25
30
35
40
45
50
0
0.02
0.04
0.06
0.08
0.1
0.12
0.14
0.16
log Mag 300kHz
Mag 300kHz
RBF2
RBF1
MET

(b)

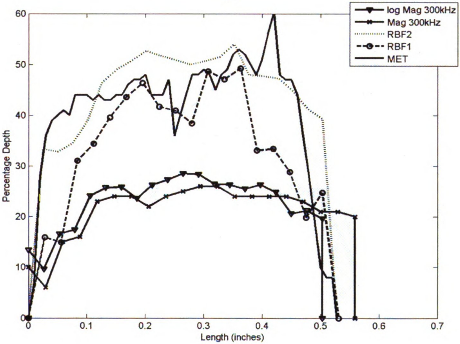

Percentage Depth
Length (inches)
0
10
20
30
40
50
60
0
0.1
0.2
0.3
0.4
0.5
0.6
0.7
log Mag 300kHz
Mag 300kHz
RBF2
RBF1
MET

(c)

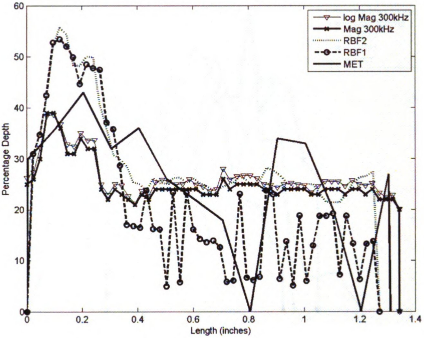
log Mag 300kHz
Mag 300kHz
RBF2
RBF1
MET
Percentage Depth
Length (inches)
0
10
20
30
40
50
60
0
0.2
0.4
0.6
0.8
1
1.2
1.4

(d)

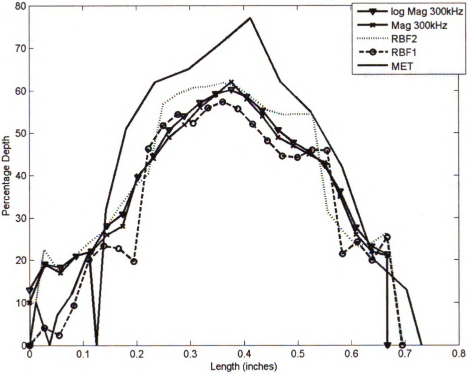
log Mag 300kHz
Mag 300kHz
RBF2
RBF1
MET
Percentage Depth
Length (inches)
0
10
20
30
40
50
60
70
80
0
0.1
0.2
0.3
0.4
0.5
0.6
0.7
0.8

(e)

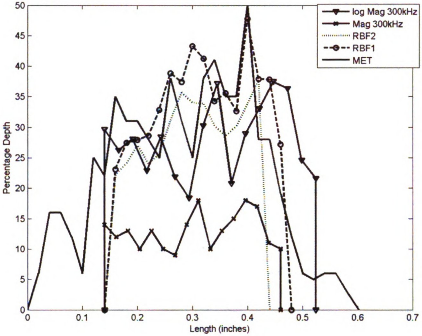

(f)

Figure 5.8(a - f) Comparison of metallographic flaw profiles with profiles generated by different algorithms.

The RBF1 and EBF2 networks are seen to consistently outperform the traditional approaches. In order to compare the effective lengths and depths of defect profiles generated using various techniques alongside the metallographic depth profile, the Electric Power Research Institute has developed two standard indices namely

- Burst Effective Length which provides an estimate of the effective length of a defect.
- Burst Effective Depth which refers to the effective defect depth.

Figures 5.9-5.11 shows the comparison of the burst effective depth and length for sample profiles obtained using the RBF neural network and the corresponding metallographic profiles.

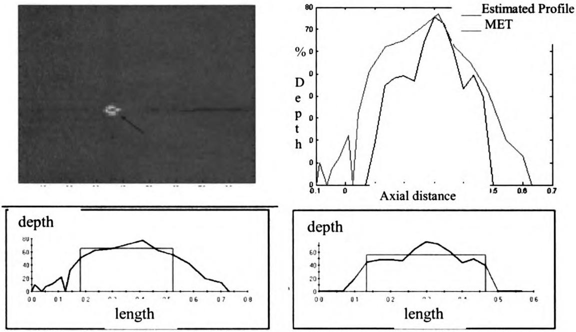

Figure 5.9 Top Left: two-dimensional representation of calibrated eddy current data signal with arrow pointing to sample training flaw indication. Top Right: Metallographic (MET) results plotted against neural network estimated depth profile. Bottom Left: Structural Profiler showing Burst Effective Length and Depth of MET (in red). Bottom Right: Structural Profiler showing Burst Effective Length and Depth of Estimated profile (in red)

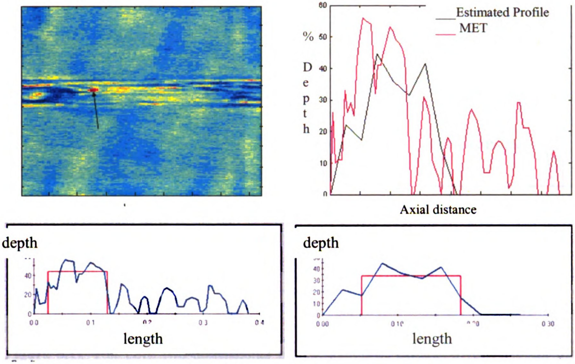

Figure 5.10 Top Left: two-dimensional representation of calibrated eddy current data signal with arrow pointing to sample training flaw indication. Top Right: Metallographic (MET) results plotted against neural network estimated depth profile. Bottom Left: Structural Profiler showing Burst Effective Length and Depth of MET (in red). Bottom Right: Structural Profiler showing Burst Effective Length and Depth of Estimated profile (in red)

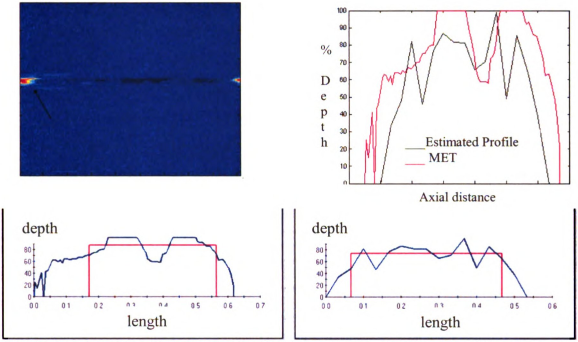

Figure 5.11 Top Left: two-dimensional representation of calibrated eddy current data signal with arrow pointing to sample training flaw indication. Top Right: Metallographic (MET) results plotted against neural network estimated depth profile. Bottom Left: Structural Profiler showing Burst Effective Length and Depth of MET (in red). Bottom Right: Structural Profiler showing Burst Effective Length and Depth of Estimated profile (in red)

Linear Regression Straight Line Fit
Slope=0.809, intercept = 16.886

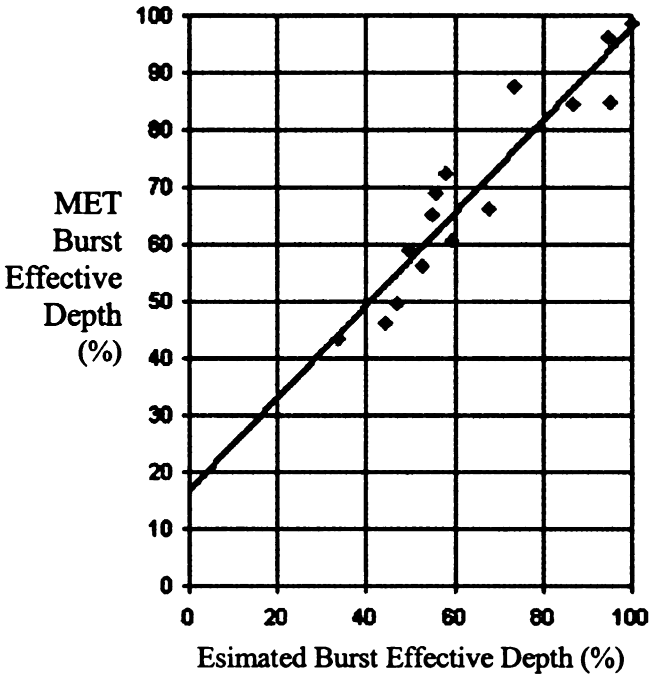

Figure 5.12(a) MET- Estimated Burst Effective Depth Correlation Statistics

Linear Regression Straight Line Fit
Slope=0.888, intercept = 3.837

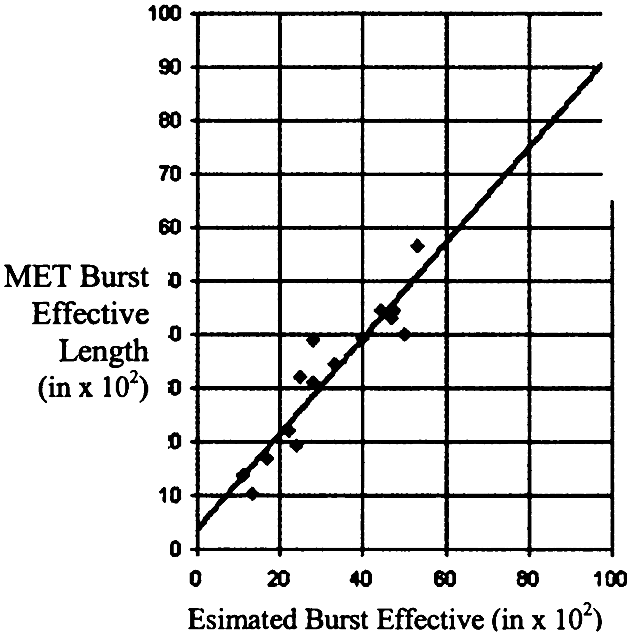

Figure 5.12(b) MET- Estimated Burst Effective Length Correlation Statistics

From figures 5.12(a) and 5.12(b), the slope of the linear fit between the pool of metallographic and estimated burst effective lengths and depths are approximately 0.93 and 0.94 respectively. This is an indication of a sufficiently trained neural network and an efficient length estimation procedure. The result in figures 5.13(a) and 5.13(b) respectively show the burst effective depth and length statistics for depth profile of test flaws generated using the radial basis function neural network (**RBF1**) and the enhanced magnitude calibration curve method.

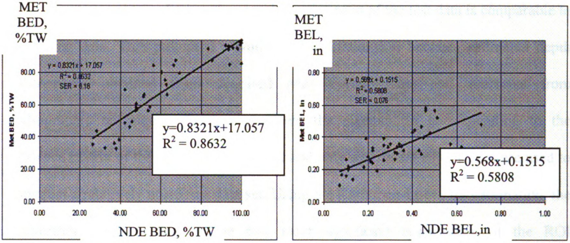

Figure 5.13(a) Performance statistics of RBF results on test data

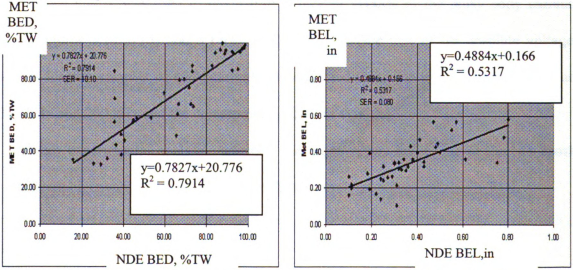

Figure 5.13(b) Performance statistics of enhanced magnitude calibration curve results on test data

The neural network outperforms the magnitude profiling procedure as the correlation of the burst effective length and depth between MET and estimated neural network depth profile are closer to unity as compared to magnitude generated results.

5.3 Uncorrelated Noise Removal in Eddy Current Data

The signal to noise ratio in eddy current data is a major factor that determines the accuracy of a predicted flaw depth profile. As it would be expected, accurate depth measurements are obtained when the signal to noise ratio of the test data is comparable to the training data. This prompted a study of the relationship between estimated depth measurements obtained from denoised eddy current data and estimates from metallographic techniques. In this approach, the eigenvalues corresponding to the covariance matrix of the ROI are determined and only significant eigenvalues are used to reconstruct a relatively noise free data set. Using the Karhunen-Loeve transformation, the eigenvectors corresponding to the two most significant eigenvalues of the ROI covariance matrix was used to reconstruct a cleaner version of the noisy eddy current data. Figures 5.14(a)-(d) and 5.14(e)-(f) show the surface plot of the absolute voltage values for two samples of eddy current data collected using the plus point coil probe at 300 kHz and 200 kHz and the corresponding filtered version.

From experimental analysis, selecting the eigenvectors belonging to the two most significant eigenvalues eliminates most of the uncorrelated signal within the ROI.

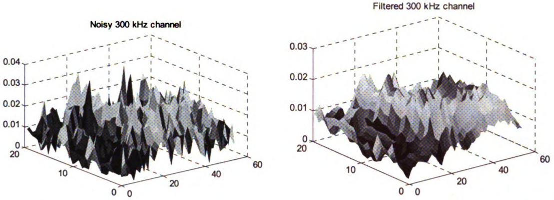

Figure 5.14(a) Magnitude values for noisy ROI in 300 kHz channel. (b) Filtered version.

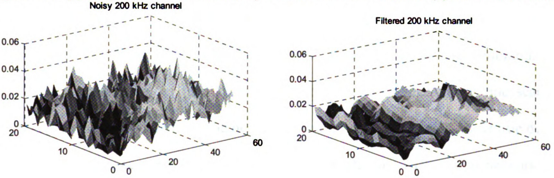

Figure 5.14(c) Magnitude values for noisy ROI in 200 kHz channel. (d) Filtered version.

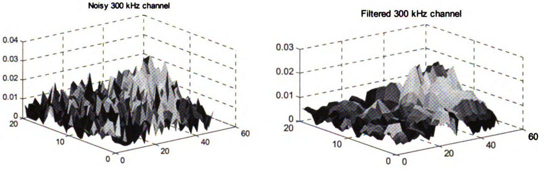

Figure 5.14(e) Magnitude values for noisy ROI in 300 kHz channel. (f) Filtered version

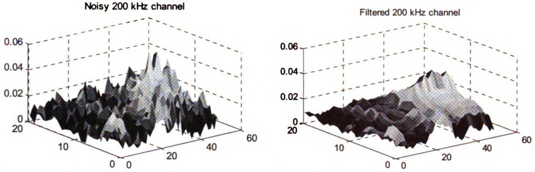
Noisy 200 kHz channel

Filtered 200 kHz channel

Figure 5.14 (g) Magnitude values for noisy ROI in 200 kHz channel. (h) Filtered version

Although, the filtered eddy current data may appear better suited to do depth profiling analysis, this is not necessarily the case. This is because the minimum and maximum magnitude values (and therefore the corresponding phase) per line scan is sometimes significantly altered in the denoising process and information about true depth is lost as a result. The depth profiles generated by the trained RBF neural network for both noisy and relatively noiseless data (which was obtained using the proposed algorithm) for those shown above are shown in figures 5.15(a) and 5.15(b).

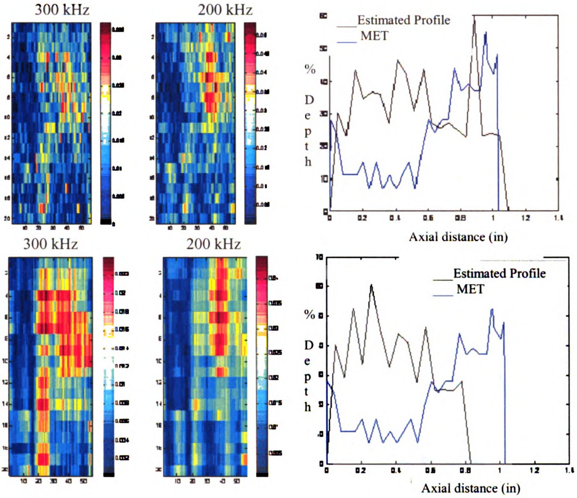

Figure 5.15(a) Top Left: Noisy ROI, Top Right: Corresponding depth profile vs. MET Bottom Left: Filtered ROI, Bottom Right: Estimated depth profile versus MET.

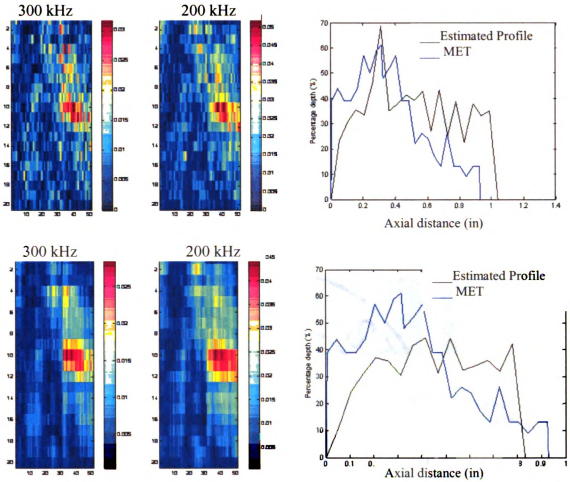

Figure 5.15(b) Top Left: Noisy ROI, Top Right: Corresponding depth profile vs. MET Bottom Left: Filtered ROI, Bottom Right: Estimated depth profile versus MET.

In order to further investigate the impact of noise on feature computation, a simulation of typical eddy current data was generated by injecting zero mean uncorrelated noise into a sample with high signal to noise ratio. Features (magnitude and phase) for each line scan in the 300 kHz channel was computed (see figures 5.17 and 5.18) and figure 5.16 shows a simulated magnitude distribution for different noise variances.

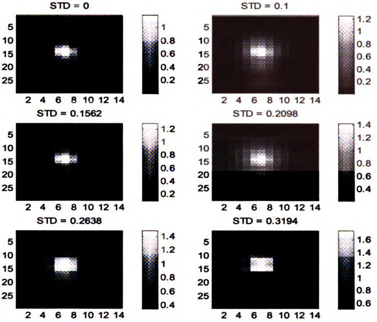

Figure 5.16 shows calibrated magnitude distribution in ROI's corrupted with zero mean noise having different levels of standard deviations (STD).

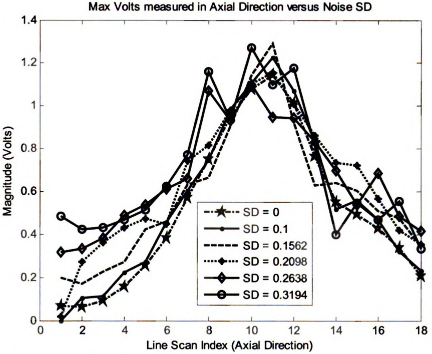

Figure 5.17 Plot of magnitude values for each circumferential line scan in ROI for various noise standard deviations.

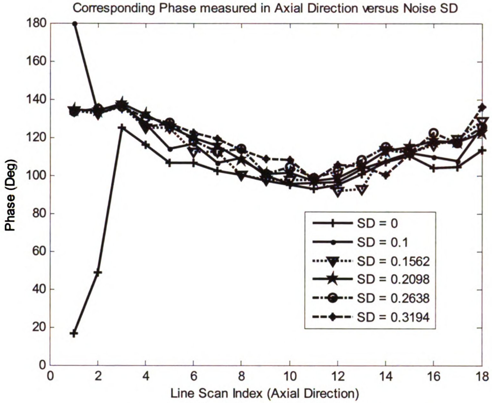

Figure 5.18 Plot of phase values for each circumferential line scan in ROI for various noise standard deviations.

The efficiency of the proposed noise elimination method was investigated on the test specimen. By introducing random uncorrelated noise with zero mean and different variance levels into the ROI and the performing the denoising operation, the depth profile for each of the resulting ROI was generated and compared with the MET profile. The depth profiles for the uncorrupted ROI and the ROI's in which random noise of known variance is introduced are plotted in figure 5.19 alongside the MET ground truth data. By inspection, it is observed that filtering the noisy ROI does not improve depth profiling results using the RBF neural network.

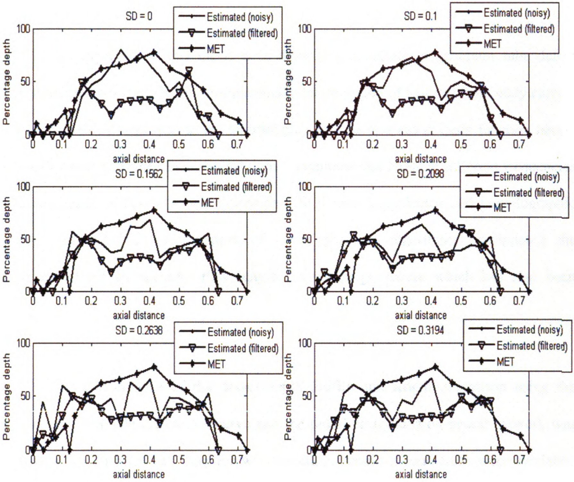

Figure 5.19 Depth profiles of MET against estimated profile generated after introducing noise of known variance and after filtering

CHAPTER 6 Conclusions and Summary

The objective of this thesis is to develop a novel steam generator tube defect characterization scheme by multi-dimensional interpolation of features from eddy current data. The vehicle deployed in the interpolation process is a radial basis function neural network which is trained by mapping signal magnitude and phase at different frequencies and contiguous slices in a two-dimensional ROI onto a predetermined metallographic depth profile (MET). Automation of depth profiling algorithms precipitated the requirement for an accurate flaw length estimation procedure which has also been developed in this project.

The performance of the defect depth profile and length estimation using the enhanced magnitude calibration curve and the radial basis function neural network was evaluated on 36 blind test data for which metallographic ground truth were available. From a linear regression perspective, the burst effective depth (BED) and length (BEL) obtained using the RBF network was more accurately correlated with the BED and BEL of the MET – having a Pearson's co-efficient of regression of 0.8632 and 0.5808 respectively. On the other hand, the Pearson's co-efficient of regression for BED and BEL using the enhanced magnitude calibration curve was 0.7914 and 0.5317 respectively. This demonstrates that the defect depth estimation procedure using neural networks in conjunction with the length estimation scheme offer a more accurate evaluation technique.

The corruption of eddy current data by noise, however, degrades the performance of the RBF network. This is largely due to the fact that the signal magnitude and phase computed as input features to the network are significantly deviant from those computed in training the network. Furthermore, the features values become more deviant from the training pattern as the signal to noise ratio increases. Filtering noisy signals is not an effective method for signal restoration since the feature information may be lost in the process. However, at low noise levels fairly consistent defect depth profiles and lengths are obtained when the novel defect characterization procedure is used. RBF1 generally performed better than RBF2 due to the significantly lower error achieved when minimizing the squared error between the predicted depth values and true depth values during the training stage (as described in equation 4.10) of RBF1 as compared to RBF2. This is expected when training with flaw signal indications with low signal to noise ratio as is typical for flaw signal indications whose corresponding maximum depth is below 40% TW. Generally, the lower the signal to noise ratio, the lesser is the absolute correlation between the signal vector and the corresponding depth value. Furthermore, it is a possibility that the contribution of depth information from neighboring horizontal slices in the ROI becomes less reliable as the signal to noise ratio decreases. This would, in turn, yield more training error in RBF2 as compared to RBF1.

Possible future work in this direction may include increasing the dimensionality of the input feature vector space for depth prediction by using flaw signal indication with significantly high signal to noise ratio and mapping four or more contiguous horizontal slices in the ROI to a depth value. In addition, training the RBF1 and RBF2 neural network with a larger database of flaw signal indications may yield more accurate depth profile estimates for a wider range of degradation types. Another potential application of the RBF neural network in depth profile estimation is to assist in the examination of cracks in other components of the steam generator such as the reactor vessels and their internal core shrouds as there have been several instances of cracking in these components [32]. Furthermore, training the RBF neural network for estimating depth profiles for other flaw types and degradations such as pitting, inter-granular attack and dents are directions worth exploring.

BIBLIOGRAPHY

1. Wenk, S.A. and R.C. McMaster. Choosing NDT: Applications, Costs and Benefits of Nondestructive Testing in Your Quality Assurance Program. Columbus, OH: American Society for Nondestructive Testing (1987).

2. McMaster, R.C. and S.A. Wenk. A Basic Guide for Management's Choice of Nondestructive Tests. Special Technical Publication No. 112. Philadelphia, PA: American Society for Testing and Materials (1951).

3. Pradeep Kumar Jella. Automated compensation and classification algorithms For array probe eddy current nondestructive evaluation. M.S. Thesis, Mich. State University, 2004

4. D. E. Bray and R. K. Stanley, Nondestructive Evaluation: A Tool for Design, Manufacturing and Service, McGraw-Hill Book Company, 1989.

5. X. Cai, Iterative Blind Deconvolution and its Application to Characterization of Eddy Current NDE Signals, M.S. Thesis, Iowa State University, 2001.

6. Automated Analysis of Rotating Probe Eddy Current Data. EPRI RPC Technical Report 2005.

7. Brian Roberts. Applying Eddy Current Inspection. Pruftechnik Technical Information Report 1999.

8. S. Haykin, Neural Networks, A Comprehensive Foundation, Macmillan, New York, 1994

9. M. Minsky and S. Papert, Perceptrons: An Introduction to Computational Geometry, MIT Press, Cambridge, MA, 1969

10. Jeannete Lawrence. Introduction to Neural Networks: Design Theory and Applications. 1994.

11. S. S. Udpa, T. Takagi, J. Pavo and R. Albanese. Electromagnetic Nondestructive Evaluation (IV) 2000.

12. Steam Generator Tubing Burst Testing and Leak Rate Testing Guidelines, EPRI Report 1006783, December 2002

13. American Society of Non-Destructive Testing: http://www.asnt.org/ndt/primer4.htm

14. Automated Analysis of Array Probe Eddy Current Data, Non-Destructive Evaluation Laboratory Technical Report November 2006.

15. William Hart Hayt, Engineering Electromagnetics Seventh Edition,(2006), McGraw Hill, New York.

16. http://www.bartleby.com/images/A4images/A4neuron.jpg.

17. http://faculty.washington.edu/chudler/synapse.html

18. http://en.wikipedia.org/wiki/Artificial_neural_network

19. Mordecai Avriel (2003). Nonlinear Programming: Analysis and Methods. Dover Publishing.

20. Kyuntae Hwang (2000), 3-D Defect Profile Reconstruction from Magnetic Flux Leakage Signatures using Wavelet Basis Function Neural Networks

21. Kenneth Moreland1 and Edward Angel, The FFT on a GPU, Graphics Hardware 2003.

22. Ameet Joshi, Inverse Problems In The Non-Destructive Evaluation Of Gas Carrying Pipelines Using Magnetic Flux Leakage, 2006

23. G. X. Ritter and J. N. Wilson, *Handbook of computer vision algorithms in image algebra*, CRC Press, New York, 1996.

24. P. Xiang, S. Ramakrishnan, X. Cai, P. Ramuhalli, R. Polikar, S. S. Udpa and L. Udpa, "Automated analysis of rotating probe multi-frequency eddy current data from steam generator tubes," *Intl. J. Applied Electromagnetics and Mechanics* (Invited paper), Vol. 12, No. 3/4, 2001, pp. 151-164

25. G. H. Ball and D. J. Hall. Some fundamental concepts and synthesis procedures for pattern recognition preprocessors. *International Conference on Microwaves, Circuit Theory, and Information Theory*, 1964.

26. . J. Barry Gomm. Selecting radial basis function network centers with recursive orthogonal least squares training. *IEEE Transactions on Neural Network*, 11:306{314, March 2000.

27. K. Z. Mao. Rbf neural network center selection based on Fisher ratio class separability measure. *IEEE Transactions on Neural Networks*, 13:1211{1216, September 2002.

28. Richard Duda, Peter Hart, and David Stork. *Pattern Classi¯cation (Second Edition)*. John Wiley & Sons, Inc., USA, 2001.

30. Simon Haykin. *Neural Networks: A Comprehensive Foundation*. Macmillan College Publishing Company, Inc., 866 Third Avenue, New York, New York 10022, 1994.

31. Rafael C. Gonzalez, Richard E. Woods. Digital Image Processing. Second Edition. Prentice Hall 2002.

32. Core Shroud Cracking at Beltline Region Welds in Boiling-Water Reactors. September 30, 1993. Nuclear Regulatory Commission -IN-93-79,

33. Pradeep Ramuhalli. Neural Network Based Iterative Algorithms For Solving Electromagnetic NDE Inverse Problems. 2002.

34. M. Yan, M Afzal, S. Udpa, S. Mandayam, Y. Sun, L. Udpa and P. Sacks, “Iteratiev algorithms for Electromagnetic NDE Signal Inversion,” ENDE ’97, September 14-16, 1997, Reggio Calabria, Italy.